

# Soil organic carbon under lockdown: Fresh plant litter as the nucleus for persistent carbon

Kristina Witzgall (✉ [kristina.witzgall@tum.de](mailto:kristina.witzgall@tum.de))

Technical University of Munich

Alix Vidal

Technical University of Munich

David Schubert

Bavarian State Research Center for Agriculture

Carmen Höschen

TU München <https://orcid.org/0000-0001-5774-2062>

Steffen Schweizer

Technical University Munich <https://orcid.org/0000-0002-9489-1005>

Franz Buegger

Institute of Biochemical Plant Pathology

Valérie Pouteau

AgroTechParis

Claire Chenu

AgroTechParis

Carsten Mueller

University of Copenhagen <https://orcid.org/0000-0003-4119-0544>

---

## Article

**Keywords:** soil organic carbon, plant litter, persistent carbon, soil matrix

**Posted Date:** February 12th, 2021

**DOI:** <https://doi.org/10.21203/rs.3.rs-156043/v1>

**License:**   This work is licensed under a Creative Commons Attribution 4.0 International License.

[Read Full License](#)

---

**Version of Record:** A version of this preprint was published at Nature Communications on July 5th, 2021.  
See the published version at <https://doi.org/10.1038/s41467-021-24192-8>.

1  
2  
3  
4  
5  
6  
7  
8  
9  
10  
11  
12  
13  
14  
15  
16  
17  
18  
19  
20  
21  
22  
23  
24  
25  
26  
27  
28

# Soil organic carbon under lockdown: Fresh plant litter as the nucleus for persistent carbon

**WITZGALL<sup>1\*</sup>, KRISTINA;** VIDAL<sup>1</sup>, ALIX; SCHUBERT<sup>2</sup>, DAVID I.; HÖSCHEN<sup>1</sup>, CARMEN;  
SCHWEIZER<sup>1</sup>, STEFFEN A.; BUEGGER, FRANZ<sup>3</sup>; POUTEAU<sup>4</sup>, VALERIE; CHENU<sup>4</sup>, CLAIRE;  
MUELLER<sup>1,5</sup>, CARSTEN W.

<sup>1</sup> Chair of Soil Science, TUM School of Life Sciences (Weihenstephan), Technical University of Munich, Freising-Weihenstephan, Germany

<sup>2</sup> Institute for Organic Farming, Soil and Resource Management, Bavarian State Research Center for Agriculture, Freising-Weihenstephan, Germany

<sup>3</sup> Institute of Biochemical Plant Pathology, Helmholtz Zentrum München (GmbH), German Research Center for Environmental Health, Neuherberg, Germany

<sup>4</sup> UMR Ecosys, AgroTechParis, Batiment EGER, Thiverval Grignon, France,

<sup>5</sup> Department for Geoscience and Environmental Management, University of Copenhagen, Copenhagen, Denmark

\*Kristina Witzgall

E-mail: [kristina.witzgall@tum.de](mailto:kristina.witzgall@tum.de)

Phone: +49 (0) 8161 71 4206

29 **Abstract**

30 The largest terrestrial organic carbon pool, carbon in soils, is regulated by the intricate connection  
31 between plant carbon inputs, microbial activity, and soil matrix. This is manifested by how  
32 microorganisms, the key players in transforming plant-derived carbon into soil organic carbon, are  
33 controlled by the physical arrangement of organic and inorganic soil particles. We studied the role of  
34 soil structure on the fate of litter-derived organic matter and we propose that the persistence of soil  
35 carbon pools is directly determined at plant–soil interfaces. We show that while microbial activity and  
36 fungal growth is controlled by soil structure, occlusion of organic matter into aggregates and formation  
37 of organo-mineral associations occur in concert on litter surfaces regardless of soil structure. These two  
38 mechanisms—the two most prominent processes contributing to the persistence of organic matter—  
39 occur directly at fresh litter that constitutes a key nucleus in the build-up of soil carbon persistence.

## 40 **Introduction**

41 Sustained by a continuous input of plant-derived carbon (C), soils comprise the largest terrestrial C pool;  
42 therefore, it has a decisive role in the global C cycle<sup>1,2</sup>. Microbial decomposition is a crucial process in  
43 transforming plant-derived organic matter (OM) and in fostering the formation of soil organic matter  
44 (SOM). Consequently, the abundance and activity of microorganisms determine the pathway of C from  
45 early-stage plant litter residues to persistent SOM<sup>3,4</sup>. In turn, the microbiome is controlled by the soil  
46 environment, where biological, chemical, and physical factors determine microbial growth and activity.  
47 One major factor for the biogeochemical functioning of soils is the 3D arrangement of solids. The  
48 physical soil structure defines the porous network, affecting the movement and bioavailability of gases  
49 (*e.g.*, CO<sub>2</sub> and O<sub>2</sub>) and water<sup>5</sup>. Determined by pore size, the differences in soil water contents can shape  
50 ecological niches suitable for certain microbial taxonomic groups. The size of pores also controls the  
51 contact between microorganisms and their essential source of energy and nutrients—the litter<sup>6</sup>. The  
52 effect of soil structure on the functionality of the microbial community can be predicted, *e.g.*, via oxygen  
53 availability, which regulates C turnover<sup>7</sup>.

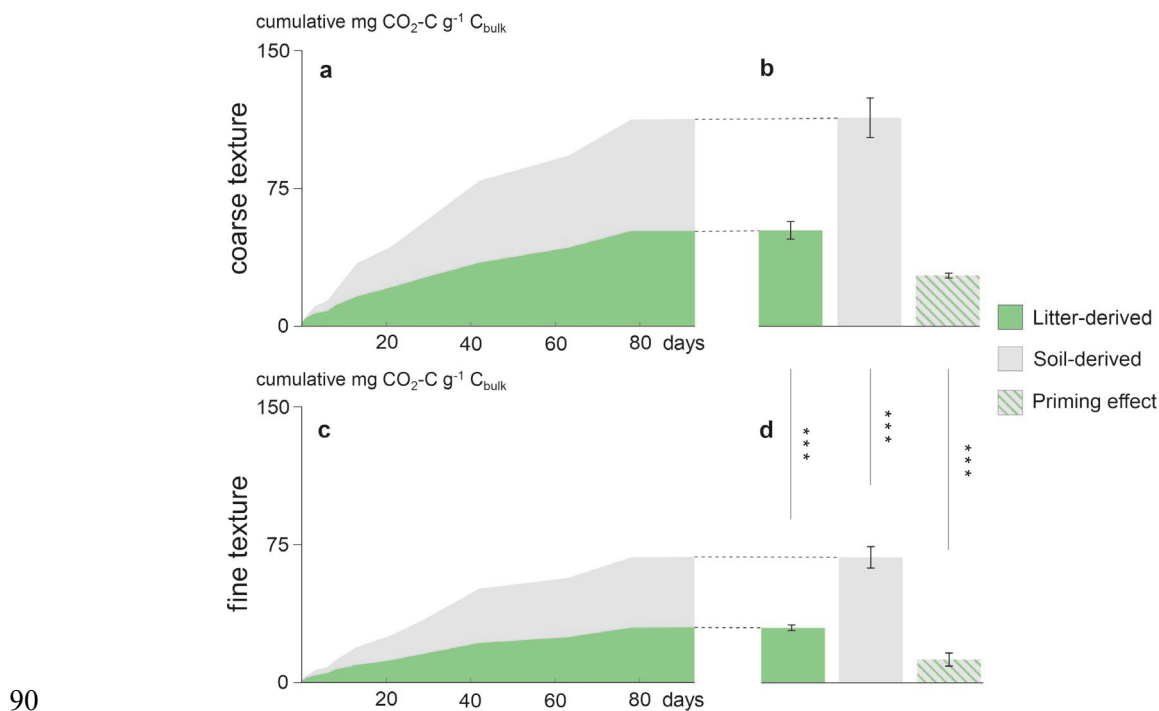
54 Over the last decades, it has become more evident that inherent recalcitrance, *i.e.*, the reduced  
55 decomposability due to the chemical composition of OM, is of less importance to SOM persistence  
56 compared to soil structure-driven mechanisms that rely on soil aggregation and accessibility of reactive  
57 mineral surfaces<sup>8,9</sup>. Soil C is mostly stored in the following two major pools: as particulate OM (POM;  
58 particulate organic residues mostly of plant origin) and mineral-associated OM (MAOM; OM adhering  
59 to mineral surfaces)<sup>10,11</sup>. Physical mechanisms, such as the potential of OM compounds to adhere to  
60 mineral surfaces<sup>12</sup>, or the accessibility of substrates for microorganisms<sup>3</sup>, are now paving the way for a  
61 better understanding of OM cycling and persistence in soils. This persistence of soil C is regulated in  
62 microscale hot spots at which microorganisms transform plant-derived OM into SOM. The functioning  
63 of biogeochemical interfaces between plant litter substrates, microorganisms, and soil mineral surfaces  
64 requires chemical, physical and biological factors to be considered in consortium.

65 We applied a systemic approach by investigating how physical soil texture governs the pathway of litter-  
66 derived C compounds from initial plant litter into more persistent SOM pools via microbial

67 transformation in a relevant process scale ( $\mu\text{m}$ – $\text{mm}$ ). To disentangle mineral-microorganism  
68 interactions that regulate these processes, we incubated two differently textured soils together with  $^{13}\text{C}$ -  
69 labeled litter in a 95-day microcosm experiment. Aside from monitoring  $\text{CO}_2$  production and litter-  
70 derived  $^{13}\text{CO}_2$  release, we followed the alterations in the chemical composition of SOM in POM and  
71 MAOM, and the microbial communities and their uptake of litter-derived  $^{13}\text{C}$  into phospholipid fatty  
72 acids (PLFA). The intact biogeochemical interfaces between plant residues, microorganisms, and soil  
73 minerals were, for the first time, directly studied using nano-scale secondary ion mass spectrometry  
74 (NanoSIMS). Our objective was to quantify the interactions between microbial litter decay and the  
75 parallel formation of more persistent soil C pools in regard to aggregate formation, and the association  
76 of microbial C with mineral surfaces controlled by soil texture.

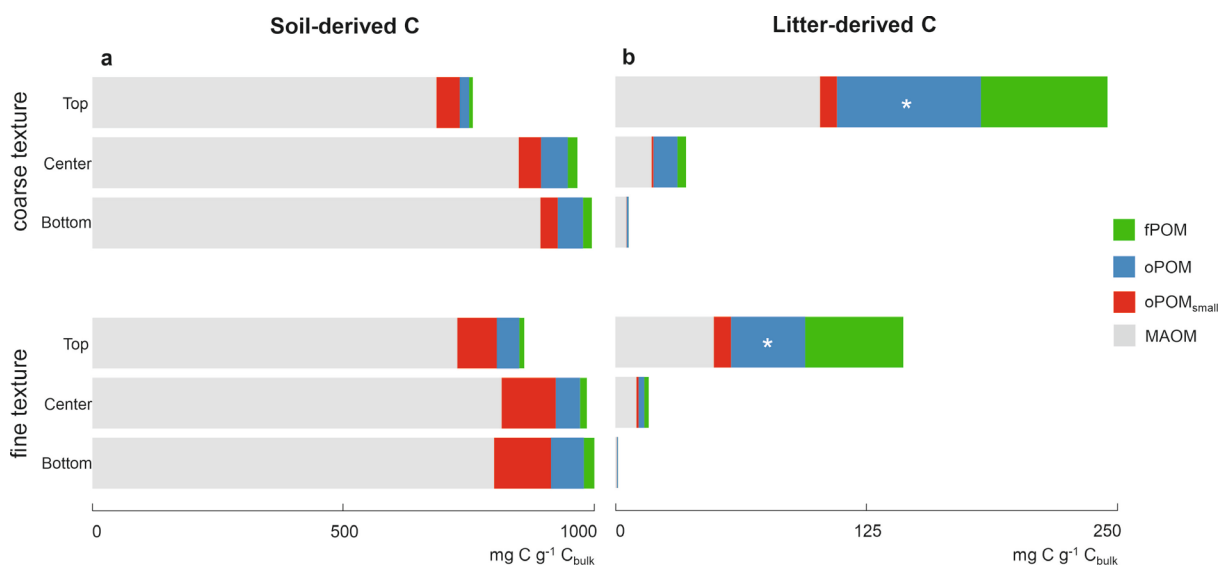
## 77 Results

78 **Litter decomposition and native soil carbon priming.** We measured how different soil textures  
79 and litter addition (enriched in  $^{13}\text{C}$ ,  $\delta^{13}\text{C} = 2129 \pm 82 \text{ ‰ V-PDB}$ ) affected the soil heterotrophic  
80 respiration by monitoring the soil- $\text{CO}_2$  emissions. By analyzing  $^{13}\text{CO}_2$ , we were able to differentiate  $\text{CO}_2$   
81 derived from native soil organic C from  $\text{CO}_2$  derived from the added litter. We report the  $\text{CO}_2$ -derived  
82 C per amount C in incubated samples to directly showcase the mechanistic process level. In the coarse-  
83 textured soil, the total native respiration ( $105.6 \text{ mg CO}_2\text{-C g}^{-1} \text{ C}_{\text{bulk}}$ ) and the net litter-derived  $\text{CO}_2$  ( $47.7$   
84  $\text{ mg CO}_2\text{-C g}^{-1} \text{ C}_{\text{bulk}}$ ) were significantly higher than in the fine-textured soil ( $65.3 \text{ mg CO}_2\text{-C g}^{-1} \text{ C}_{\text{bulk}}$   
85 and  $29.0 \text{ mg CO}_2\text{-C g}^{-1} \text{ C}_{\text{bulk}}$ ,  $p < 0.001$ ,  $t = -7.512$  and  $t = -6.593$  respectively;  $df = 8$  for both, Fig. 1).  
86 While the litter-derived  $\text{CO}_2$  accounted for around 30% of the total respiration in both soil textures, the  
87 litter addition induced a higher total priming effect in the coarse-textured soil (Fig. 1 b and d), accounting  
88 for a net release of  $27.5 \text{ mg CO}_2\text{-C g}^{-1} \text{ C}_{\text{bulk}}$  from the native soil organic C in the coarse-textured soil  
89 compared to  $12.8 \text{ mg CO}_2\text{-C g}^{-1} \text{ C}_{\text{bulk}}$  in the fine-textured soil ( $p < 0.001$ ,  $t = -7.686$ ,  $df = 8$ ).



91 **Figure 1 | Cumulative heterotrophic respiration in fine- and coarse-textured soil.** a Respired  $\text{CO}_2\text{-C g}^{-1} \text{ C}_{\text{bulk}}$   
92 during the 95-day incubation in a, b coarse-textured, and c, d fine-textured soil. The total respired  $\text{CO}_2\text{-C}$  in soil with b coarser and d finer texture is displayed on the right (means, SDs displayed with errors bars,  $n = 5$ ), together with the total priming effect. Asterisks represent significant differences between the textures (\*\*\*) ( $p < 0.001$ ).

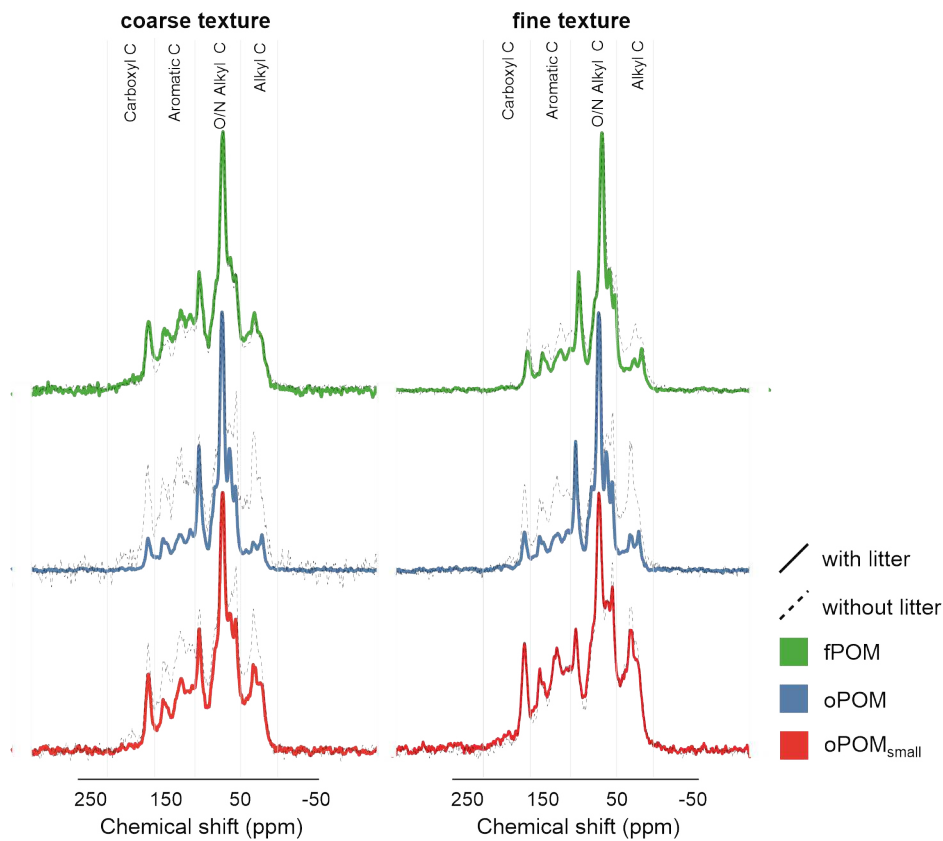
96 **Fate of litter-derived carbon in particulate and mineral-associated OM fractions.** We  
 97 assessed the contribution of OC derived from the decaying litter to the formation of differently stabilized  
 98 OM pools in two soils with contrasting textures divided into three depths (top, center, and bottom) by  
 99 soil fractionation according to density and size. The soil-derived C in  $\text{mg C g}^{-1} \text{C}_{\text{bulk}}$  was similarly  
 100 distributed across OM fractions for both differently structured soils. The MAOM fraction dominated the  
 101 C storage in both soils (Fig. 2 a). In the coarse-textured soil, we found a significantly higher litter-  
 102 derived C content occluded within aggregates (oPOM) ( $71.1 \text{ mg C g}^{-1} \text{C}_{\text{bulk}}$  compared to  $36.8 \text{ mg C g}^{-1}$   
 103  $\text{C}_{\text{bulk}}$  in the fine-textured soil,  $p = 0.007$ ,  $t = -5.03$ ,  $df = 4$ ) and a slightly higher content in the MAOM  
 104 fraction ( $101.3 \text{ mg C g}^{-1} \text{C}_{\text{bulk}}$  in the soil with coarser texture compared to  $48.8 \text{ mg C g}^{-1} \text{C}_{\text{bulk}}$  in the soil  
 105 with finer texture,  $p = 0.08$ ,  $W = 0$ ) (Fig. 2 b). Although not statistically significant, a tendency of a  
 106 higher contribution of litter-derived C recovered as oPOM and MAOM in the coarse-textured soil further  
 107 extended down with soil depth to the center layer of the microcosms ( $p = 0.06$  in both cases,  $t = -2.66$   
 108 and  $-2.60$ , respectively;  $df = 4$  for both).



109 **Figure 2 | Allocation of soil- and litter-derived C to OM fractions.** Content of free POM (fPOM),  
 110 occluded POM (oPOM, oPOM<sub>small</sub>) and mineral-associated OM (MAOM) in  $\text{mg C g}^{-1} \text{C}_{\text{bulk}}$  of **a** soil and  
 111 **b** litter origin in three depths of coarse- and fine-textured soil (means,  $n = 3$ ). Asterisks represent  
 112 significant differences between the textures ( $*p < 0.05$ ).  
 113

114 **Fresh litter incorporated into soil aggregate structures.** The chemical composition of OM  
 115 fractions was analyzed using  $^{13}\text{C}$  solid-state nuclear magnetic resonance spectroscopy (NMR).  
 116 Carbohydrates (O/N alkyl C) clearly dominated the NMR spectra of all fPOM fractions (Fig. 3), and a  
 117

118 similar chemical composition was also detected in oPOM fractions of both textures with litter. In oPOM  
 119 fractions, the added litter had induced an increase in relative intensity from around 50% to 70% in the  
 120 O/N-alkyl C region, demonstrating the dominance of polysaccharides (mainly cellulose and  
 121 hemicellulose)<sup>13</sup>. According to the molecular mixing model results, this was further supported by the  
 122 relative increase in carbohydrates (26% in the coarse- and 20% in the fine-textured soil) accompanied  
 123 by a relative decrease in lignin (-12% in the coarse- and -20% in the fine-textured soil) in oPOM  
 124 fractions<sup>14,15</sup>. The incorporation of litter-derived OC into soil aggregate structures was also demonstrated  
 125 by the decrease in aliphaticity (alkyl:O/N alkyl ratio) in oPOM compared to control samples.



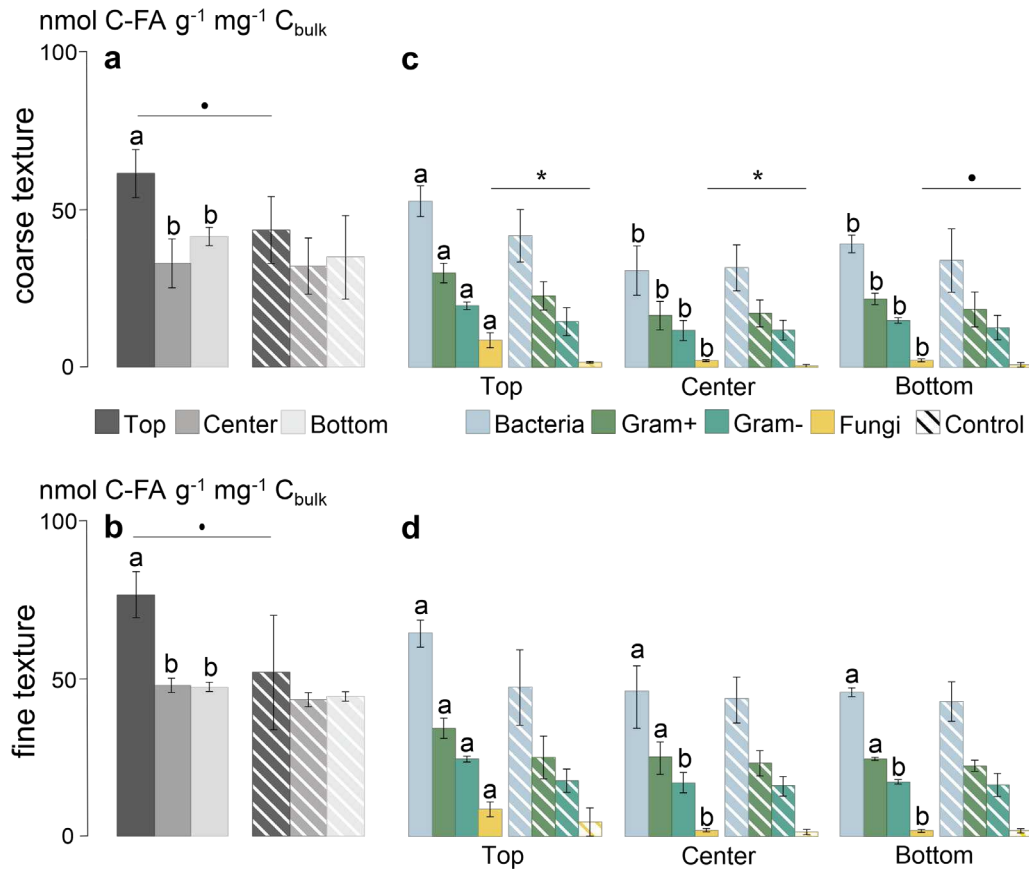
126

127 **Figure 3 | Differences in the chemical composition of particulate OM fractions.** Solid-state <sup>13</sup>C-  
 128 MAS NMR spectra displaying the chemical compositions of free POM (fPOM) and occluded POM  
 129 (oPOM, oPOM<sub>small</sub>) in coarse- and fine-textured soil (control samples in black). The chemical shift  
 130 regions represent the following functional groups: 0-45 ppm (alkyl C), 45-110 ppm (O/N alkyl C), 110-  
 131 160 ppm (aromatic C), and 160-220 ppm (carboxyl C). n = 3 for the following fractions: fPOM with litter  
 132 (both textures), oPOM with litter (both textures), oPOM<sub>small</sub> with litter in the finer texture. For the rest of  
 133 the samples, n = 1.

134

135 **Fungi respond the strongest to litter addition.** The changes caused by litter addition in microbial  
136 community structures between the textures were captured via the measurement of microbial-derived  
137 PLFA. The litter amendment led to a slight increase in the total PLFA content in the top layers of both  
138 the coarse- ( $61 \text{ nmol g}^{-1} \text{ mg soil C}^{-1}$ ,  $p = 0.07$ ,  $t = -2.40$ ,  $df = 4$ ) and fine-textured soil ( $76 \text{ nmol g}^{-1} \text{ mg}$   
139  $\text{soil C}^{-1}$ ,  $p = 0.1$ ,  $t = -2.15$ ,  $df = 4$ ), whereas the total PLFA contents in the center and bottom layers  
140 were similar to those of the controls (Fig. 4 a and b). While the differences in soil texture had no effect  
141 on the overall community structure, a strong response to litter addition was detected in fungal  
142 biomarkers. The increase in fungal markers was particularly pronounced in the top layer of the coarse-  
143 textured soil where fungal abundance increased by a factor of 5.4 ( $p = 0.01$ ,  $t = -4.11$ ,  $df = 4$ ) compared  
144 to 2.6 in the fine-textured soil ( $p = 0.15$ ,  $t = -1.75$ ,  $df = 4$ ). As opposed to the other observed microbial  
145 groups, the increase in fungal markers also extended into the center layer of microcosms with coarse-  
146 textured soil ( $2.1 \text{ nmol g}^{-1} \text{ mg soil C}^{-1}$  compared to  $0.4 \text{ nmol g}^{-1} \text{ mg soil C}^{-1}$  in the control,  $p = 0.02$ ,  $t$   
147  $= -3.81$ ,  $df = 4$ ) (Fig. 4 c), while there was no corresponding increase in the respective layers in the  
148 finer-textured soil (Fig. 4 d).

149



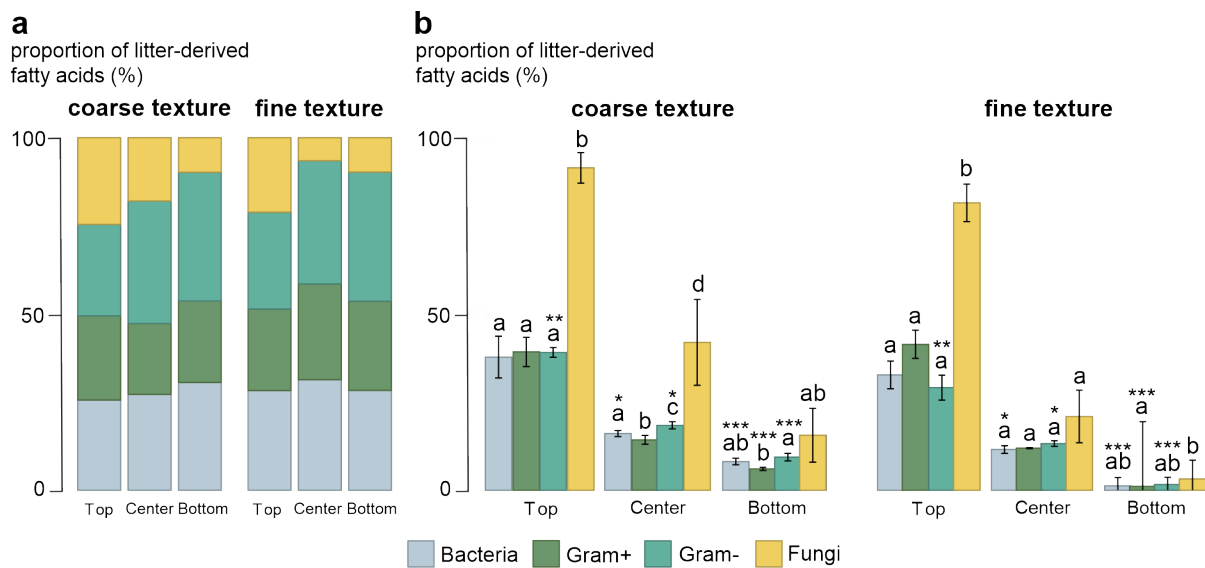
150

151 **Figure 4 | Community structures and functionality of microorganisms.** The total abundance of  
 152 phospholipid fatty acids (PLFA) normalized for bulk C in nmol C-FA g<sup>-1</sup> mg<sup>-1</sup> C<sub>bulk</sub> (means, SDs displayed  
 153 with errors bars, n = 3) in soil with **a** coarser and **b** finer texture, divided into four microbial subgroups in  
 154 **c** coarse- and **d** fine-textured soil. Significance levels indicated by dots and asterisks (\*p < 0.1, \*p < 0.05)  
 155 represent the differences between the litter treatment and controls, and lowercase letters represent the  
 156 significant (p < 0.05) differences between the layers. Control samples are displayed as hatched.

157

158 When considering the proportion of fatty acids with incorporated litter-derived <sup>13</sup>C within the observed  
 159 groups in relation to the total amount of enriched FAs in the sample, neither texture nor depth had an  
 160 effect (Fig. 5 a). This corroborated the consistent community structures detected during the PLFA  
 161 analysis. When considering the C proportions of <sup>13</sup>C-enriched FAs to unlabeled FAs within each microbial  
 162 group, the proportion was by far the highest in the fungal markers (92% in the coarser- and 82% in finer-  
 163 textured soil, p = 0.11 between textures, t = -2.04, df = 4, Fig. 5 b). This distinction of fungi compared  
 164 to other microbial groups was significant in top layers of both textures, as well as in the center layer of  
 165 the coarse-textured soil (over 42% of FAs were enriched compared to 21% in the fine-textured soil).  
 166 Furthermore, the proportion of enriched gram-negative markers were significantly higher in all layers

167 of the coarser-textured soil ( $p = 0.004$ ,  $t = -5.79$ ,  $p = 0.019$ ,  $t = -3.83$ , and  $p = 0.0007$ ,  $t = -9.54$ ;  $df = 4$   
 168 for all) compared to the fine-textured soil.



169

170 **Figure 5 | Litter incorporation in microbial biomass.** **a** The proportion of litter-derived fatty acids  
 171 within a certain microbial group related to the total amount of litter-enriched fatty acids in the entire  
 172 sample (%) in the three depths of two textures (means,  $n = 3$ ). **b** The proportion of  $^{13}\text{C}$ -enriched fatty  
 173 acids compared to unlabeled fatty acids within each microbial group (%) in the three depths of two  
 174 textures (means, SDs displayed with errors bars,  $n = 3$ ). Lowercase letters represent the significant  
 175 differences ( $p < 0.05$ ) between microbial groups and asterisks (\* $p < 0.05$ , \*\* $p < 0.01$ , \*\*\* $p < 0.001$ )  
 176 represent the differences between textures. Differences between depths were significant in all groups.

177

178 **Formation of MAOM fostered by microbial activity on decaying POM surface.** We gained

179 a direct insight on the biogeochemical interface between decaying plant residues (POM), mineral

180 particles, and microorganisms at the microscale using scanning electron microscopy (SEM) and

181 NanoSIMS. Large areas of litter-derived POM particles were covered in  $^{13}\text{C}$ -enriched microbial-derived

182 extracellular polymeric substances (EPS), forming a biofilm-like structure that was intertwined with

183 fungal hyphae and unicellular microorganisms (presumably bacteria). Clay-sized minerals were directly

184 enclosed into the biofilm on the POM surface (Fig. 6 a and b). The microorganisms and EPS were

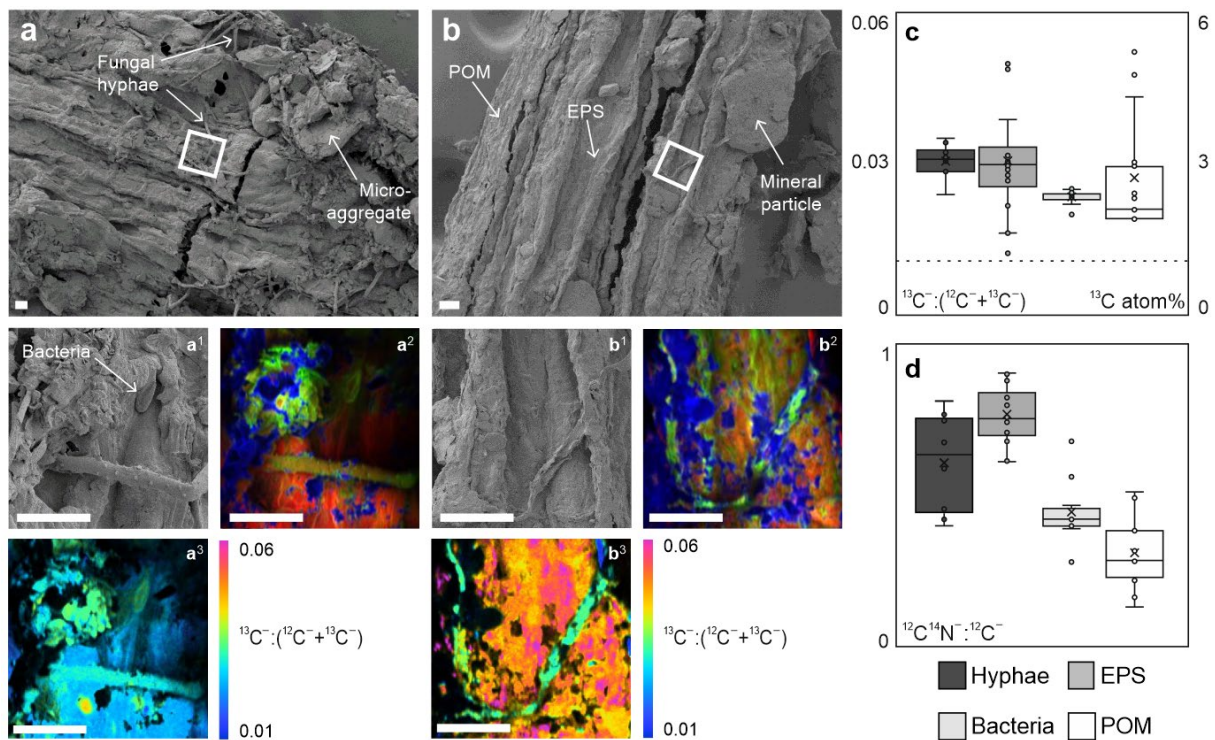
185 significantly enriched in N compared to the underlying POM, with a higher  $^{12}\text{C}^{14}\text{N} : ^{12}\text{C}$  ratio obtained

186 for EPS, followed by hyphae and bacteria (Fig. 6 d). The  $^{13}\text{C}^- : (^{12}\text{C}^- + ^{13}\text{C}^-)$  ratios for fungal hyphae,

187 bacteria, and EPS (3.0, 2.3 and 3.0 atom %  $^{13}\text{C}$ , respectively) were well over the natural abundance level

188 (1.1 atom %  $^{13}\text{C}$ ), and the hyphae showed a significantly higher enrichment compared to bacteria and

189 POM ( $p < 0.05$ ,  $df = 3$ , Fig. 6 c).



190  
191  
192  
193  
194  
195  
196  
197  
198  
199  
200  
201  
202  
203  
204  
205  
206  
207

**Figure 6 | High  $^{13}\text{C}$  enrichment detected in fungal hyphae and EPS based on NanoSIMS imaging.** Scanning electron microscopy (SEM) images of  $^{13}\text{C}$ -enriched maize litter incubated in microcosms and isolated as particulate organic matter (POM) in **a** coarse- and **b** fine-textured soil. **a<sup>1</sup>/b<sup>1</sup>** SEM micrographs of measurement spots in **(a<sup>1</sup>)** coarse- and **(b<sup>1</sup>)** fine-textured soil, which were later analyzed by nano-scale secondary ion mass spectrometry (NanoSIMS). **a<sup>2</sup>/b<sup>2</sup>** NanoSIMS composite images displayed as RGB (Red =  $^{12}\text{C}^-$ , Green =  $^{12}\text{C}^{14}\text{N}^-$  and Blue =  $^{16}\text{O}^-$ ). **a<sup>3</sup>/b<sup>3</sup>** NanoSIMS hue-saturation intensity (HIS) images displaying the  $^{13}\text{C}^-:(^{12}\text{C}^- + ^{13}\text{C}^-)$  isotope ratios of POM, fungal hyphae and extracellular polymeric substances (EPS) in the coarse- and fine-textured soil. Here the enrichment level is displayed as HIS images with a color scale ranging from natural abundance (0.011) in blue to high enrichment in purple (0.065). Scale bars represent 10  $\mu\text{m}$ . **c** Boxplots of  $^{13}\text{C}^-:(^{12}\text{C}^- + ^{13}\text{C}^-)$  isotope ratios and **d**  $^{12}\text{C}^{14}\text{N}^-:^{12}\text{C}^-$  ratios of hyphae (n = 8), EPS (n = 16), bacteria (n = 10), and POM (n = 13) in both textures obtained by NanoSIMS (medians, error bars denote data ranging between the 5<sup>th</sup> and 95<sup>th</sup> percentiles). The natural abundance of  $^{13}\text{C}$  is indicated by the hatched line. The regions of interest were selected manually on continuous fragments of hyphae, individual bacteria, patches of EPS and exposed POM surfaces. Significant differences ( $p < 0.05$ ) between the four groups are indicated by lowercase letters.

208  
209

210

## 211 **Discussion**

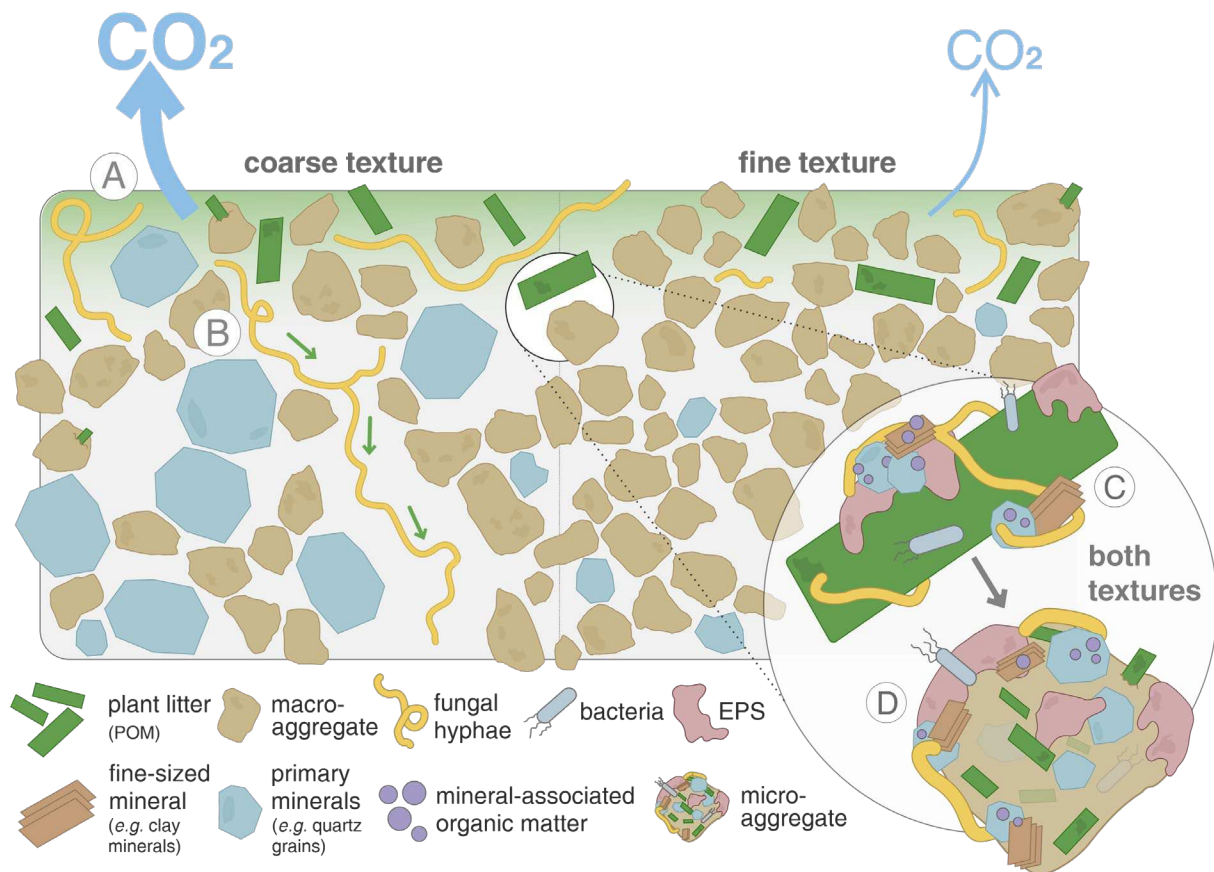
212 Soil texture, and thus the 3D structure of soils, controls overall microbial activity; the coarser soil texture  
213 entailed both higher decomposition of litter-derived OM, and an increased priming effect, fostering the  
214 mineralization of native soil C (Fig. 1 b and d). Plant litter fragments located in larger soil pores of  
215 coarse-textured soils are more easily accessible; therefore, litter decomposition is enhanced<sup>16-18</sup>. In the  
216 coarse-textured soil, the increased accessibility and, hence, increased bioavailability of litter-derived C  
217 was further demonstrated by consistently higher proportions of labeled PLFAs in gram-negative bacteria  
218 across all soil depths (Fig. 5 b); bacteria that are specialized in the processing of labile plant C  
219 sources<sup>19,20</sup>.

220 We show that the coarse-textured soil offered a more favorable habitat for fungi in a micro-environment  
221 rich in bioavailable substrates formed by fresh unprotected litter. Fungal abundance increased by more  
222 than five-fold following the litter addition in the coarse-textured soil. Furthermore, a substantial part (92  
223 % in the coarse-textured soil) of the fungal biomass was directly derived from the added plant litter, as  
224 demonstrated by the PLFA profiles (labeled PLFA profiles; Fig. 5 b). This highlights the key role of the  
225 fungal community for rapid litter decomposition, particularly in coarse-textured soils. Soil structure with  
226 a distinct soil pore network determines the abundance and community structure of microbiota<sup>21</sup>. Fungi  
227 are mainly found in macropore spaces (> 10  $\mu\text{m}$ ) that are noticeably larger than the hyphae itself<sup>6,22,23</sup>.  
228 The filamentous growth of the mycelium enables fungi to bridge air-filled pore spaces, supporting them  
229 to overcome capillary boundaries between wet and dry soil, and to adapt to heterogeneous pore  
230 networks<sup>24-26</sup>. Consequently, under the physical conditions of coarse-textured soils, fungi have a clear  
231 advantage over other microorganisms to reach OM in hard-to-access soil compartments that are not  
232 connected via water nor biofilms<sup>21</sup>. We stress that in sandy soils, fungi are key to sustain crucial soil  
233 functions such as C and nutrient cycling by the transformation of litter-derived OM into SOM.

234 In the coarse-textured soil, fungal activity extended away from the litter source, thereby promoting a  
235 downward transfer of litter-derived C into deeper soil layers (PLFA depth profiles; Fig. 4). This pattern  
236 can partly be attributed to the apical properties of the fungal mycelium, enabling the translocation of C  
237 sources throughout the fungal colony<sup>27-29</sup>. The expansion of hyphal networks facilitates the incorporation

238 of litter into aggregates<sup>30,31</sup>. The stabilization of aggregated soil structures can be ascribed to the  
239 exudation of EPS (*e.g.*, polysaccharides, Fig. 6 a and b) from the hypha<sup>32</sup>. We propose that the expansion  
240 of fungal hyphae, together with its interactions with mineral particles, results in the build-up of litter-  
241 derived oPOM in the deeper soil layers away from the litter source (Fig. 2 b). This intricate interaction  
242 between fungal hyphae, plant residues, and mineral particles adhering to microbial-derived EPS was  
243 underlined by spectromicroscopic imaging (Fig. 6). With the direct measurement of intact plant-fungi  
244 interfaces, we emphasize the key role of fungi in the translocation of litter-derived C within soils, as  
245 well as in the formation of aggregates and mineral-associated OM—a process which ultimately drives  
246 the stabilization of litter-derived C compounds in soils.

247 We were able to demonstrate the incorporation of plant C into microbial biomass directly in the interface  
248 of plant residues and soil minerals. This was quantified with high levels of <sup>13</sup>C enrichment in fungal  
249 hyphae and microbial EPS on the POM surface (Fig. 6). The direct contact between minerals (<sup>16</sup>O<sup>-</sup>  
250 distribution; Fig. 6) and microbial biomass (<sup>12</sup>C<sup>14</sup>N<sup>-</sup>; Fig. 6), together with the enmeshment of fresh litter  
251 (free POM) with fungal hyphae and microbial-derived EPS (Fig. 6 a and b), promotes the gluing of fine-  
252 sized soil minerals. This agglomeration of fine mineral particles, driven by microbial activity and  
253 regulated by the bioavailability of litter-derived C, drives aggregate formation and soil structure  
254 development directly at the plant–soil interface. In addition, the chemical composition of the litter-  
255 derived OM that got entrapped in soil aggregates (oPOM) by this soil structure formation resembled the  
256 undecomposed litter (Fig. 3). Thus, particulate OM acts as an important precursor for aggregate  
257 formation and parallel occlusion of litter-derived POM into aggregated soil structures (Fig. 7).



258

259 **Figure 7 | Aggregate and mineral-associated organic matter formation in soils of different**  
 260 **textures driven by interactions between litter, microorganisms and soil matrix.** Fresh litter  
 261 surfaces serve as hotspots of microbial activity driving the formation of organo-mineral associations in  
 262 concert with comprising a nucleus for aggregate formation. **(A)** Coarse soil texture fosters higher  
 263 mineralization of native and litter-derived organic matter resulting in higher  $\text{CO}_2$  emissions compared to  
 264 the fine-textured soil. **(B)** Fungal hyphae in coarse-textured soils promote the translocation of litter-  
 265 derived C away from the litter source. **(C)** Regardless of texture, gluing of fine-sized minerals, driven by  
 266 microbial products (EPS) on the fresh litter surface lead to **(D)** the formation of soil aggregates directly  
 267 at the plant–soil interface.

268 Regardless of soil texture, fresh litter surfaces serve as hotspots of microbial activity driving the  
 269 formation of organo-mineral associations in concert with comprising a nucleus for aggregate formation.  
 270 Thus, the biogeochemical interfaces of decaying plant litter determine—via promoted microbial  
 271 activity—the two most prominent mechanisms which increase the persistence of OC in soils; the *(i)*  
 272 occlusion of POM in soil aggregates and *(ii)* the association of OM with mineral surfaces as  
 273 simultaneous universal processes across soils of different structure (Fig. 7). These two mechanisms  
 274 strongly rely on the spatial proximity of particulate litter and its surfaces, microbial residues, and fine-  
 275 sized mineral particles. Thus, the formation of persistent POM and MAOM, both constituting soil  
 276 organic C pools with low turnover times<sup>4,10</sup>, is directly fueled by the decomposition of POM and  
 277 controlled by microbial activity.

## 278 **Methods**

### 279 **Study site and soil sampling**

280 Soil was collected in December 2017 at 5–20 cm (Ap horizon) from an agricultural field located in  
281 Southern Germany (Freising, Bavaria, 48°23'53.8"N, 11°38'39.7"E). The sampling area is situated  
282 within the lower Bavarian upland, and characterized by a mean annual temperature of 7.8 °C and mean  
283 annual precipitation of 786 mm. The soil type is a Cambisol (silty clay loam; 32% clay, 53% silt, and  
284 14% sand) with a considerable amount of loess mixed with underlying Neogene sandy sediments. The  
285 collected soil was oven-dried (2 days, 40 °C), sieved (< 2 mm), and visible plant remains were manually  
286 removed using tweezers.

### 287 **Experimental setup**

288 The experimental design involved four treatments; soils of two textures, either with or without <sup>13</sup>C-  
289 labeled maize stalks. In order to obtain a coarse-textured soil (sandy clay loam; 24% clay, 15% silt, and  
290 60% sand), half of the initial soil was mixed with quartz sand (Quarzwirke, Frechen, Germany).  
291 Approximately 120 g (for coarser texture) and 90 g (for finer texture) of soil was filled homogeneously  
292 and gently packed (bulk density 0.9–1.3 g cm<sup>-3</sup>) into microcosms (polymethylene; height: 5 cm, internal  
293 diameter: 5 cm, total volume: 98.2 cm<sup>3</sup>). While the control microcosms were filled entirely with soil,  
294 330 mg of air-dried and grounded <sup>13</sup>C-labeled maize stalks (2–3 mm, δ<sup>13</sup>C = 2129 ± 82 ‰ V-PDB;  
295 Agroscope, Zurich, Switzerland) were mixed into the upper 1.67 cm of the soil within the other  
296 microcosms to create a quasi-natural gradient, with aboveground litter addition from the top. Each of  
297 the four treatments was replicated five times. The microcosms were sealed from below with polyester  
298 gauzes (37-µm mesh) and placed into Ball Mason Jars (475 mL) on top of metal grids to ensure  
299 downward gas diffusion.

### 300 **Heterotrophic respiration**

301 After making all containers gas-tight and rinsing them with synthetic air (Westfalen AG, Münster,  
302 Germany), 12 mL of gas samples (IVA Analysentechnik, Meerbusch, Germany) were collected from  
303 the headspace of the Mason Jars on day 2, 3, 4, 8, 10, 15, 23, 31, 44, 65, 80, and 95. For each  
304 measurement of CO<sub>2</sub> respiration, two samplings of container atmosphere were carried out, and the time  
305 in-between the two samplings was adapted to the current respiration rates. During the incubation period

306 of 95 days, the CO<sub>2</sub> concentration, as well as the <sup>13</sup>C abundance in the respired CO<sub>2</sub>, was measured via  
307 gas chromatography isotope ratio mass spectrometry (GC/IRMS) (Delta Plus, Thermo Fisher, Dreieich,  
308 Germany). The CO<sub>2</sub> levels were calibrated against three calibration gases (890, 1500 and 3000 ppm  
309 CO<sub>2</sub>; Linde AG, Pullach, Germany). Then, source carbonic acid with known isotopic composition  
310 diluted in helium was used as a lab standard. This standard was in turn calibrated against three  
311 international standards (RM 8562, RM 8563, and RM 8564; International Atomic Energy Agency,  
312 Vienna, Austria) with a dual inlet system. The temperature and water holding capacity were kept  
313 constant at 21 °C and 60%, respectively, along with the incubation period.

### 314 **Sampling**

315 After 95 days of incubation, each microcosm was cut into three horizontal sections with a razor blade,  
316 separating the top, center, and bottom layer (each 1.67-cm high). Subsamples for subsequent microbial  
317 analyses were freeze-dried and stored at 4 °C, and dried aliquots for fractionation were stored in sealed  
318 plastic containers at 20 °C. Furthermore, a few POM particles were selected manually for NanoSIMS  
319 measurements.

### 320 **Physical fractionation and subsequent analyses**

321 The soil was separated into five distinct OM fractions using a combined density and particle size  
322 fractionation scheme<sup>33</sup>. Air-dried soil (18–20 g) was gently capillary-saturated with sodium  
323 polytungstate solution (Na<sub>6</sub>[H<sub>2</sub>W<sub>12</sub>O<sub>40</sub>]; 1.8 g cm<sup>-3</sup>) and after 12 h, the free-floating particulate organic  
324 matter (fPOM) was collected using a vacuum pump. oPOM was released from aggregated soil structures  
325 via ultrasonic dispersion (Bandelin, Sonoplus HD 2200; energy input of 440 J ml<sup>-1</sup>) allowing its  
326 separation from heavier minerals. The excess salt was removed from the oPOM by washing it with  
327 deionized water over a sieve (20-µm mesh size), which yielded an oPOM fraction of < 20 µm  
328 (oPOM<sub>small</sub>). Both fPOM and oPOM fractions were washed for several times using deionized water and  
329 pressure filtration (20-µm mesh) until the solution dropped below an electric conductivity of < 5 µS/cm  
330 via pressure filtration. The oPOM<sub>small</sub> fraction was cleaned via saturation with deionized water for 24 h.  
331 While sand and coarse silt fractions were separated by wet sieving, mineral fractions < 20 µm were  
332 separated via sedimentation, and later combined as one MAOM fraction. The C, N, and <sup>13</sup>C contents  
333 were determined for freeze-dried and milled OM fractions, as well as milled bulk soil, via dry

334 combustion with an isotope ratio mass spectrometer (Delta V Advantage, Thermo Fisher, Dreieich,  
 335 Germany) coupled with an elemental analyzer (Euro EA, Eurovector, Milano, Italy). Acetanilide was  
 336 used as a lab standard for calibration and to determine the isotope linearity of the system, and was in  
 337 turn calibrated against several suitable isotope standards (International Atomic Energy Agency, Vienna,  
 338 Austria). International and lab isotope standards were included in every sequence to create a final <sup>13</sup>C  
 339 correction. Since the samples did not contain carbonates, the C contents were assumed to be equal to  
 340 organic C contents.

### 341 <sup>13</sup>C Nuclear Magnetic Resonance Spectroscopy

342 The chemical compositions of the POM fractions were determined via <sup>13</sup>CP-MAS NMR in solid state  
 343 (Bruker DSX 200, Bruker BioSpin GmbH, Karlsruhe, Germany), where samples were filled into 7-mm  
 344 zirconium dioxide rotors and spun in a magic angle spinning probe at a rotation speed of 6.8 kHz and  
 345 0.01024 s acquisition time. The recorded <sup>13</sup>C spectra were quantified in the following chemical shift  
 346 regions: alkyl C (-10–45 ppm), O alkyl C (45–110 ppm), aromatic C (110–160 ppm), and  
 347 carbonyl/carboxyl C (160–220 ppm)<sup>33</sup>. The regions were integrated and an alkyl C/O alkyl C ratio (-10–  
 348 45/45–110 ppm) was computed to describe the degree of aliphaticity of the different fractions<sup>34</sup>. Lastly,  
 349 the obtained spectra were transformed into OM compound classes via the molecular mixing model<sup>15,35</sup>  
 350 with the following chemical shift regions: 0–45, 45–60, 60–95, 95–110, 100–145, 145–165 and 165–  
 351 215 ppm.

### 352 Calculations of litter-derived C in CO<sub>2</sub>, soil and OM fractions

353 Along with the incubation period, the amount of C respired per hour was computed as

$$354 \quad \frac{mg \text{ CO}_2 - C}{h} = \frac{\Delta \text{CO}_2}{\Delta t} \left[ \frac{ppm}{min} \right] \cdot \frac{1}{10^6} \cdot \frac{V_{HSP} [ml]}{22.4 \left[ \frac{ml}{mmol} \right] \cdot \frac{T_0 [K]}{T_1 [K]}} \cdot 12 \left[ \frac{mg \text{ CO}_2 - C}{mmol} \right] \cdot 60 \text{ min}$$

355 where ΔCO<sub>2</sub>/Δt is CO<sub>2</sub> increase over time, V<sub>HSP</sub> is the volume of the headspace of Mason Jars. The  
 356 volume of an ideal gas is set at 22.4, and 12 represents the atomic mass of C.

357 Subsequently, the percentage of respired CO<sub>2</sub> originating from the litter was calculated as

358 
$$CO_2C_{litter}[\%] = \left( \frac{\delta^{13}C_{resp} - \delta^{13}C_{control}}{\delta^{13}C_{litter} - \delta^{13}C_{control}} \right) \cdot 100$$

359 where  $\delta^{13}C_{resp}$  emission gives the  $\delta^{13}C$  for the current  $CO_2$  emission between the two samplings (‰ V-  
 360 PDB),  $\delta^{13}C_{control}$  is the average  $\delta^{13}C$  of the control soils at the time of measurement, and  $\delta^{13}C_{litter}$  is the  
 361  $\delta^{13}C$  signature of the labeled litter. Finally, the respired C originating from the soil was computed as

362 
$$CO_2-C_{soil}[\%] = 100 - CO_2-C_{litter}$$

363 The proportion of litter-derived C (%) in the OM fractions was calculated<sup>36</sup> as

364 
$$Litter - derived C [\%] = \frac{\delta^{13}C_{labeled} - \delta^{13}C_{control}}{\delta^{13}C_{litter} - \delta^{13}C_{control}} \cdot 100$$

365 where  $\delta^{13}C_{labeled}$  is the  $^{13}C$  enrichment in labeled samples,  $\delta^{13}C_{control}$  is the  $^{13}C$  enrichment in controls  
 366 (natural abundance level, *i.e.*, 28 ‰ V-PDB), and  $\delta^{13}C_{litter}$  is the  $^{13}C$  enrichment in the added litter (*i.e.*,  
 367 2129 ‰ V-PDB) from which the amount of litter-derived C within each OM fraction could then be  
 368 determined as

369 
$$C_{litter} [mg] = \frac{litter - derived C}{100} \times C_{fraction} \times m$$

370 where  $C_{fraction}$  is the amount of C in  $mg\ g^{-1}$ , and  $m$  is the recovered mass (g) of each fraction after the  
 371 fractionation.

372 **PLFA analyses**

373 The PLFA patterns were analyzed<sup>37</sup> and adjusted according to the ISO/TS 29843-2:2011F standard. In  
 374 summary, the soil lipids from 3 g of soil (freeze-dried aliquots) were extracted with a Bligh & Dyer  
 375 solution [methanol, chloroform, and citrate buffer (pH = 4 ± 0.1), 2:1:0.8, v/v/v]. A biphasic system was  
 376 achieved by adding chloroform and citrate buffer from which the lipid phase was evaporated at 30 °C  
 377 under a nitrogen stream. The phospholipids were separated from neutral lipids and glycolipids by solid-  
 378 phase extraction on silica tubes (SPE DSC-Si, 500 mg, Discovery<sup>®</sup>) and evaporated. The PLFA were  
 379 turned into fatty acid methyl esters (FAMES) via alkaline methanolysis<sup>38</sup> and later quantified via gas

380 chromatographic retention time comparison with a gas chromatograph (GC Agilent HP6890, G1530A,  
 381 Chemstation, Santa Clara, USA) connected to a flame ionization detector equipped with a capillary  
 382 column (SGE, BPX5, 60 m × 0,25 mm × 0,25 mm). The FAME concentrations were quantified relative  
 383 to methyl nonadecanoate (19:0), enabling methylated lipids to be identified. A standard soil was used  
 384 and extracted in parallel to detect potential deviations between the extraction rounds, expressed in nmol  
 385 C-FA per g of soil. Mono-unsaturated and cyclopropylated PLFA (C16:1w7c, C18:1w9c, and  
 386 C18:1w9t) were assigned to gram-negative bacteria, iso- and anteiso-branched PLFA (iC15:0, aC15:0,  
 387 iC16:0, i-C17:0, C:17, and C18:0) were assigned to gram-positive bacteria and C18:2w6c, C18:3w3c  
 388 respectively C20:5w3c were assigned to fungi<sup>39</sup>. The total content of bacteria was expressed by adding  
 389 gram-positive, gram-negative together with the markers C14:0, C16:0, C20:0, and C15:1. Lastly, the  
 390 <sup>13</sup>C-labeling of FAME was concluded by correcting for the added methyl moieties during methanolysis  
 391 and relating it to the chain length of fatty acids

$$392 \quad \delta^{13}C_{FA} [\text{‰ } V - PDB] = \frac{(C_n + 1) \times \delta^{13}C_{FAME} - \delta^{13}C_{MeOH}}{C_n}$$

393 where  $\delta^{13}C_{FA}$  represents the  $\delta^{13}C$  of the fatty acid,  $C_n$  the number of C atoms in the fatty acid,  $\delta^{13}C_{FAME}$   
 394 is the  $\delta^{13}C$  of the fatty acid methyl ester, and  $\delta^{13}C_{MeOH}$  is the  $\delta^{13}C$  of the methanol used for the  
 395 methylation (-63 ‰) to calculate the isotope ratios of the fatty acids. The relative incorporation of <sup>13</sup>C  
 396 into four microbial groups was calculated by relating the proportions of each fatty acid to the total <sup>13</sup>C  
 397 incorporation, and the absolute incorporation of <sup>13</sup>C in each microbial group was calculated by dividing  
 398 the amount of <sup>13</sup>C enriched fatty acid with the total amount of extracted fatty acid for that particular  
 399 group.

#### 400 **SEM and NanoSIMS microspectroscopy**

401 In order to gain insights on the microscale distribution of the assemblages of litter with microbes and  
 402 minerals, we used SEM and NanoSIMS. Free POM from non-fractionated soil was hand-picked and  
 403 fixed onto graphene sample substrates on metal stubs (10 mm in diameter). To avoid the charging  
 404 phenomena, samples were gold-coated prior to SEM analyses by physical vapor deposition under argon  
 405 atmosphere (Emitech Sputtercoater SC7620, Gala Instrumente, Bad Schwalbach, Germany). To analyze

406 the microscale structures of the assemblages of POM, microorganisms and soil minerals of the samples  
407 were first analyzed using SEM (Jeol JSM 5900LV, Freising, Germany), and subsequently the spots that  
408 best exemplified the microbial transformation on the decaying litter (POM) surface were analyzed using  
409 a Cameca NanoSIMS 50 L (Cameca, Gennevilliers, France)<sup>40</sup>. For the NanoSIMS measurements, a 270-  
410 pA high primary beam was used to locally sputter away impurities and gold coating, and to implant  
411 primary ions ( $\text{Cs}^+$ ) into the samples surface (impact energy of 16 keV) to enhance the yields of secondary  
412 ions. Subsequently, secondary ions were measured using electron multipliers;  $^{12}\text{C}^-$ ,  $^{13}\text{C}^-$ ,  $^{12}\text{C}^{14}\text{N}^-$  to  
413 display OM fragments and  $^{16}\text{O}^-$ ,  $^{28}\text{Si}^-$ ,  $^{27}\text{Al}^{16}\text{O}^-$  and  $^{56}\text{Fe}^{16}\text{O}^-$  secondary ions to record the mineral phase.  
414 The instrument was tuned to a high mass resolution in order to accurately separate mass isobars at mass  
415 13 ( $^{13}\text{C}^-$ ,  $^{12}\text{C}^{1}\text{H}^-$ ). The ion images were acquired with a  $25 \times 25 \mu\text{m}$  field of view, 40 planes and 1 ms  
416  $\text{pixel}^{-1}$  dwell time for all measurements. Charging effects were compensated for with an electron flood  
417 gun if necessary. The acquired measurements were dead time (44 ns) and drift corrected using the  
418 OpenMIMS plugin of the ImageJ software. The  $^{13}\text{C}^-:(^{12}\text{C}^- + ^{13}\text{C}^-)$  and  $^{12}\text{C}^{14}\text{N}^-:^{12}\text{C}^-$  ratios were computed  
419 for distinct regions of interests which were chosen manually with respect to the major compartments:  
420 continuous fragments of fungal hyphae, individual bacteria, EPS patches as well as exposed POM  
421 surfaces. To account for instrumental mass fractionation, the electron multipliers were carefully  
422 checked, and the control measurements of non-labeled POM samples were conducted regularly along  
423 the sessions. Here, the mean  $^{13}\text{C}^-:(^{12}\text{C}^- + ^{13}\text{C}^-)$  ratios were in line with the level of natural abundance,  
424 which meant that a correction of ratios for labeled POM samples was not necessary.

## 425 **Statistical analyses**

426 All parameters were separately tested for normality with Shapiro–Wilk test and for homoscedasticity  
427 with Bartlett’s test. In addition, the distribution of the datasets was checked with Q-Q plots. In cases  
428 where the assumptions of normality or homoscedasticity were not met, a log-transformation was applied  
429 on the raw data and analyses were carried out on the log-transformed data. The differences caused by  
430 texture and litter addition were tested using unpaired t tests, and depth differences were tested using  
431 one-way analysis of variance with Tukey’s honestly significant difference as the post-hoc test. In cases  
432 where the log-transformed data did not meet the requirements for parametrical testing, the unpaired two-  
433 samples Wilcoxon test or Kruskal-Wallis test was applied. The statistical findings were considered

434 significant if the confidence limits were in excess of 95% ( $p < 0.05$ ). All statistical testing was carried  
435 out in the R statistical environment<sup>41</sup> using agricolae<sup>42</sup> and ggpubr<sup>43</sup> packages.

436

## 437 **Acknowledgements**

438 The authors gratefully acknowledge the support by the Deutsche Forschungsgemeinschaft (DFG)  
439 through grant no. HO 5121/1-1. We are thankful to Gertraud Harrington and Johann Lugmeier for their  
440 technical assistance related to the NanoSIMS measurements, Maria Greiner for the laboratory assistance  
441 and Isabel Prater for support with the  $^{13}\text{C}$ -NMR Spectroscopy measurement and evaluation. Further, we  
442 thank Juliane Hirthe for providing the  $^{13}\text{C}$ -labeled maize litter and Josef Reischenbeck for preparing  
443 equipment for the incubation. Authors also acknowledge Dominik Fiedler from Fraunhofer Society for  
444 the support on the SEM analyses. We are grateful for the financial support of the Centre de Cooperation  
445 Universitaire Franco-Bavarois for Bavarian-French cooperation for research (FK13-2018) as well as the  
446 DFG funding received for the NanoSIMS instrument [KO 1035/38-1].

## 447 **Author contributions**

448 KW carried out the measurements following the incubation, collected and analyzed data, and wrote the  
449 manuscript; AV designed and supervised the experiment and wrote the manuscript; DIS designed and  
450 conducted the incubation and respiration measurements, prepared samples for subsequent analyses and  
451 collected and analyzed data; CH conducted the NanoSIMS measurements and supported the data  
452 evaluation; SS designed and supported the incubation experiment and contributed to the data evaluation  
453 of the NanoSIMS measurements; FB conducted and evaluated the GC-IRMS measurements of  $\text{CO}_2$  and  
454 the EA-IRMS measurements of soil fractions; VP supervised the PLFA extraction, conducted the GC-  
455 C-IRMS measurements and evaluated the data, JH provided the labeled plant litter; CC supervised the  
456 PLFA and PLFA-SIP extraction and evaluated the data; CWM designed and supervised the experiment  
457 and wrote the manuscript. All authors discussed the data and contributed to the final draft.

## 458 **Data availability**

459 The data supporting the findings of this study are available on request from the corresponding author  
460 (KW).

## 461 **Competing financial interests**

462 The authors declare no competing financial interests.

## 463 **References**

- 464 1. Friedlingstein, P. *et al.* Global carbon budget. *Earth Syst. Sci. Data* **11**, 1783–1838 (2019)
- 465 2. Lal, R. Beyond COP 21: potential and challenges of the “4 per Thousand” initiative. *J. Soil Water*  
466 *Conserv.* **71**, 20A–25A (2016)
- 467 3. Lehmann, J. *et al.* Persistence of soil organic carbon caused by functional complexity. *Nature* **13**,  
468 529–534 (2020)
- 469 4. Cotrufo, M. F., Wallenstein, M. D., Boot, C. M., Deneff, K. & Paul, E. The Microbial Efficiency-  
470 Matrix Stabilization (MEMS) framework integrates plant litter decomposition with soil organic matter  
471 stabilization: do labile plant inputs form stable soil organic matter? *Glob. Change Biol.* **19**, 988–995  
472 (2013)
- 473 5. Young, I. M., Crawford, J. W., Nunan, N., Otten, W. & Spiers, A. Microbial distribution in soils:  
474 physics and scaling. *Adv. Agron.* **100**, 81–121 (2008)
- 475 6. Lennon, J. T., Aanderud, Z. T., Lehmkuhl, B. K. & Schoolmaster D. R., Jr. Mapping the niche space  
476 of soil microorganisms using taxonomy and traits. *Ecology.* **93**, 1867–1879 (2012)
- 477 7. Keiluweit, M., Nico, P. S., Kleber, M. & Fendorf, S. Are oxygen limitations under recognized  
478 regulators of organic carbon turnover in upland soils? *Biogeochemistry.* **127**, 157–171 (2016)
- 479 8. Dungait, J. A. J., Hopkins, D. W., Gregory, A. S. & Whitmore, A. P. Soil organic matter turnover is  
480 governed by accessibility not recalcitrance. *Glob Change Biol.* **18**, 1781–1796 (2012)
- 481 9. Schmidt, M. W. I. *et al.* Persistence of soil organic matter as an ecosystem property. *Nature* **478**, 49–  
482 56 (2011)
- 483 10. Mueller, C. W. & Kögel-Knabner, I. Soil organic carbon stocks, distribution, and composition  
484 affected by historic land use changes on adjacent sites. *Biol. Fertil. Soils* **45**, 347–359 (2009)
- 485 11. Lavalley, J. M., Soong, J. L. & Cotrufo, M. F. Conceptualizing soil organic matter into particulate  
486 and mineral-associated forms to address global change in the 21<sup>st</sup> century. *Glob. Change Biol.* **26**, 261–  
487 273 (2019)
- 488 12. Kleber, M. *et al.* Mineral-organic associations: formation, properties, and relevance in soil  
489 environments. *Adv. Agron.* **130**, 1–140 (2015)
- 490 13. Kölbl, A. & Kögel-Knabner, I. Content and composition of free and occluded particulate organic  
491 matter in a differently textured arable Cambisol as revealed by solid-state <sup>13</sup>C NMR spectroscopy. *J.*  
492 *Plant Nutr. Soil Sci.* **167**, 45–53 (2004)
- 493 14. Baldock, J. A., Masiello, C. A., Gélinas, Y. & Hedges, J. I. Cycling and composition of organic  
494 matter in terrestrial and marine ecosystems. *Mar. Chem.* **92**, 39–64 (2004)
- 495 15. Nelson, P. N. & Baldock, J. A. Estimating the molecular composition of a diverse range of natural  
496 organic materials from solid-state <sup>13</sup>C NMR and elemental analyses. *Biogeochemistry.* **72**, 1–34 (2005)
- 497 16. Strong, D. T., Wever, H. D. E., Merckx, R. & Recous, S. Spatial location of carbon decomposition  
498 in the soil pore system. *Eur. J. Soil Sci.* **55**, 739–750 (2004)

- 499 17. Nunan, N. The microbial habitat in soil: scale, heterogeneity and functional consequences. *J. Plant*  
500 *Nutr. Soil Sci.* **180**, 425–429 (2017)
- 501 18. Steffens, M. *et al.* Identification of distinct functional microstructural domains controlling C storage  
502 in soil. *Environ. Sci. Technol.* **51**, 12182–12189 (2017)
- 503 19. Kramer, C. & Gleixner, G. Soil organic matter in soil depth profiles: distinct carbon preferences of  
504 microbial groups during carbon transformation. *Soil Biol. Biochem.* **40**, 425–433 (2008)
- 505 20. Fanin, N., Hättenschwiler, S. & Fromin, N. Litter fingerprint on microbial biomass, activity, and  
506 community structure in the underlying soil. *Plant Soil.* **379**, 79–91 (2014)
- 507 21. Erktan, A., Or, D. & Scheu, S. The physical structure of soil: determinant and consequence of trophic  
508 interactions. *Soil Biol. Biochem.* **148**, 107876 (2020)
- 509 22. Schack-Kirchner, H., Wilpert, K. V. & Hildebrand, E. E. The spatial distribution of soil hyphae in  
510 structured spruce-forest soils. *Plant Soil.* **224**, 195–205 (2000)
- 511 23. Harris, K., Young, I. M., Gilligan, C. A., Otten, W. & Ritz, K. Effect of bulk density on the spatial  
512 organisation of the fungus *Rhizoctonia solani* in soil. *FEMS Microbiol. Ecol.* **44**, 45–56 (2003).
- 513 24. Adu, J. K. & Oades, J. M. Utilization of organic materials in soil aggregates by bacteria and fungi.  
514 *Soil Biol. Biochem.* **10**, 117–122 (1978)
- 515 25. De Boer, Wd., Folman, L. B., Summerbell, R. C. & Boddy, L. Living in a fungal world: impact of  
516 fungi on soil bacterial niche development. *FEMS Microbiol. Rev.* **29**, 795–811 (2005)
- 517 26. Guhr, A., Marzini, C., Borken, W., Poll, C. & Matzner, E. Effect of water redistribution by two  
518 distinct saprotrophic fungi on carbon mineralization and nitrogen translocation in dry soil. *Soil Biol.*  
519 *Biochem.* **103**, 380–387 (2016)
- 520 27. Killham, K. *Soil Ecology*. (Cambridge: Cambridge University Press, 1994)
- 521 28. Frey, S. D., Six, J. & Elliott, E. T. Reciprocal transfer of carbon and nitrogen by decomposer fungi  
522 at the soil-litter interface. *Soil Biol. Biochem.* **35**, 1001–1004 (2003)
- 523 29. Poll, C., Ingwersen, J., Stemmer, M., Gerzabek, M. H. & Kandeler, E. Mechanisms of solute  
524 transport affect small-scale abundance and function of soil microorganisms in the detritusphere. *Eur. J.*  
525 *Soil Sci.* **57**, 583–595 (2006)
- 526 30. Baumert, V. L. *et al.* Root exudates induce soil macroaggregation facilitated by fungi in subsoil.  
527 *Front. Environ. Sci.* **6**:140 (2018)
- 528 31. Vidal, A. *et al.* Linking 3D soil structure and plant-microbe-soil carbon transfer in the rhizosphere.  
529 *Front. Environ. Sci.* **6**:9 (2018)
- 530 32. Costa, O. Y. A., Raaijmakers, J. M. & Kuramae, E. E. Microbial extracellular polymeric substances:  
531 ecological function and impact on soil aggregation. *Front. Microbiol.* **9**:1636 (2018)
- 532 33. Mueller, C. W. & Kögel-Knabner, I. Soil organic carbon stocks, distribution, and composition  
533 affected by historic land use changes on adjacent sites. *Biol. Fertil. Soils.* **45**, 347–359 (2009)

- 534 34. Baldock, J. A. *et al.* Assessing the extent of decomposition of natural organic materials using solid-  
535 state  $^{13}\text{C}$  NMR spectroscopy. *Aust. J. Soil Res.* **35**, 1061–1083 (1997)
- 536 35. Prater, I. *et al.* From fibrous plant residues to mineral-associated organic carbon—the fate of organic  
537 matter in Arctic permafrost soils. *Biogeosciences* **17**, 3367–3383 (2020)
- 538 36. Comeau, L. P., Lemke, R. K., Knight, J. D. & Bedard-Haughn, A. Carbon input from  $^{13}\text{C}$ -labeled  
539 crops in four soil organic matter fractions. *Biol. Fert. Soils.* **49**, 1179–1188 (2013)
- 540 37. Frostegård, Å., Bååth, E. & Tunlio, A. Shifts in the structure of soil microbial communities in limed  
541 forests as revealed by phospholipid fatty acid analysis. *Soil Biol. Biochem.* **25**, 723–730 (1993).
- 542 38. Kramer, S., Marhan, S., Haslwimmer, H., Ruess, L. & Kandeler, E. Temporal variation in surface  
543 and subsoil abundance and function of the soil microbial community in an arable soil. *Soil Biol.*  
544 *Biochem.* **61**, 76–85 (2013)
- 545 39. Quideau, S. A. *et al.* Extraction and analysis of microbial phospholipid fatty acids in soils. *J. Vis.*  
546 *Exp.* **114**: 54360 (2016)
- 547 40. Mueller, C. W. *et al.* Chapter one—Advances in the analysis of biogeochemical interfaces:  
548 NanoSIMS to investigate soil microenvironments. *Adv. Agron.* **121**, 1–46 (2013)
- 549 41. R Core Team. R: A Language and Environment for Statistical Computing. *R foundation for*  
550 *statistical computing* <http://www.R-project.org/> (2020)
- 551 42. De Mendiburu, F. *Agricolae*: Statistical procedures for agricultural research. R package version 1.3–  
552 3, Available from: <https://CRAN.R-project.org/package=agricolae>, 2020
- 553 43. Kassambara, A. *Ggpubr*: ‘Ggplot2’ based publication ready plots. R package version 0.4.0. Availble  
554 from: <https://CRAN.R-project.org/package=ggpubr>, 2020

# Figures

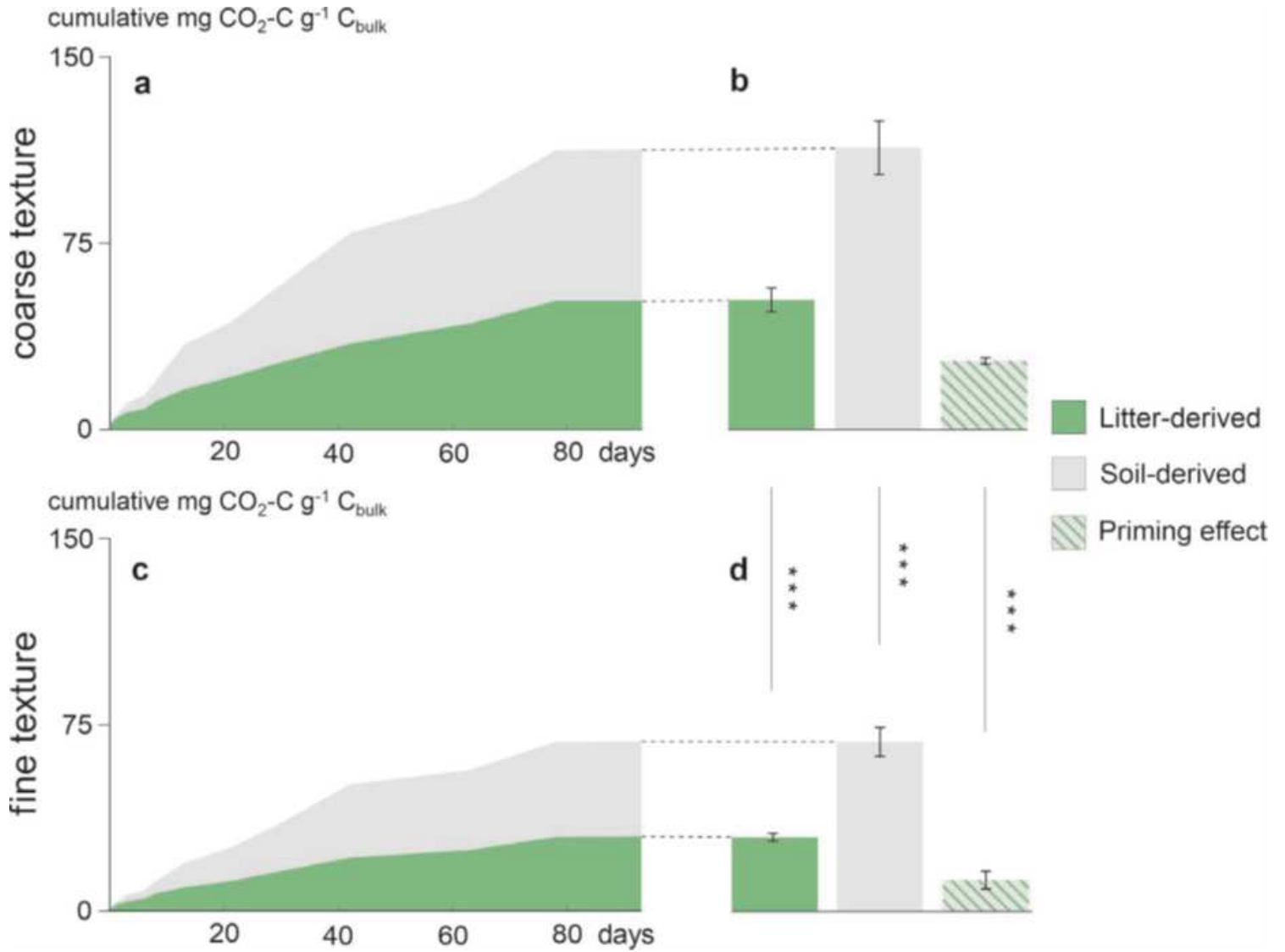


**Figure 1**

Cumulative heterotrophic respiration in fine- and coarse-textured soil. a Respired CO<sub>2</sub>-C g<sup>-1</sup> C<sub>bulk</sub> during the 95-day incubation in a, b coarse-textured, and c, d fine-textured soil. The total respired CO<sub>2</sub>-C in soil with b coarser and d finer texture is displayed on the right (means, SDs displayed with errors bars, n = 5), together with the total priming effect. Asterisks represent significant differences between the textures (\*\*\*p < 0.001).

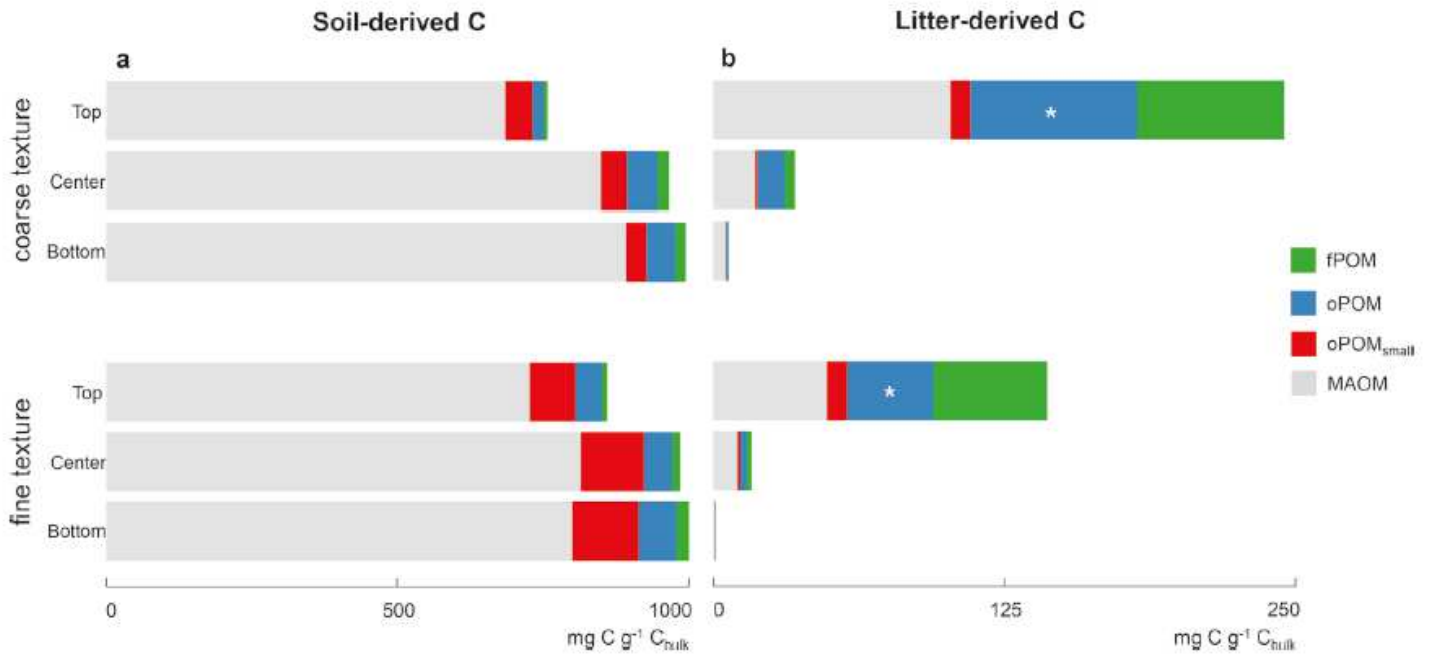


**Figure 2**

Allocation of soil- and litter-derived C to OM fractions. Content of free POM (fPOM), occluded POM (oPOM, oPOM<sub>small</sub>) and mineral-associated OM (MAOM) in mg C g<sup>-1</sup> C<sub>bulk</sub> of a soil and b litter origin in three depths of coarse- and fine-textured soil (means, n = 3). Asterisks represent significant differences between the textures (\*p < 0.05).

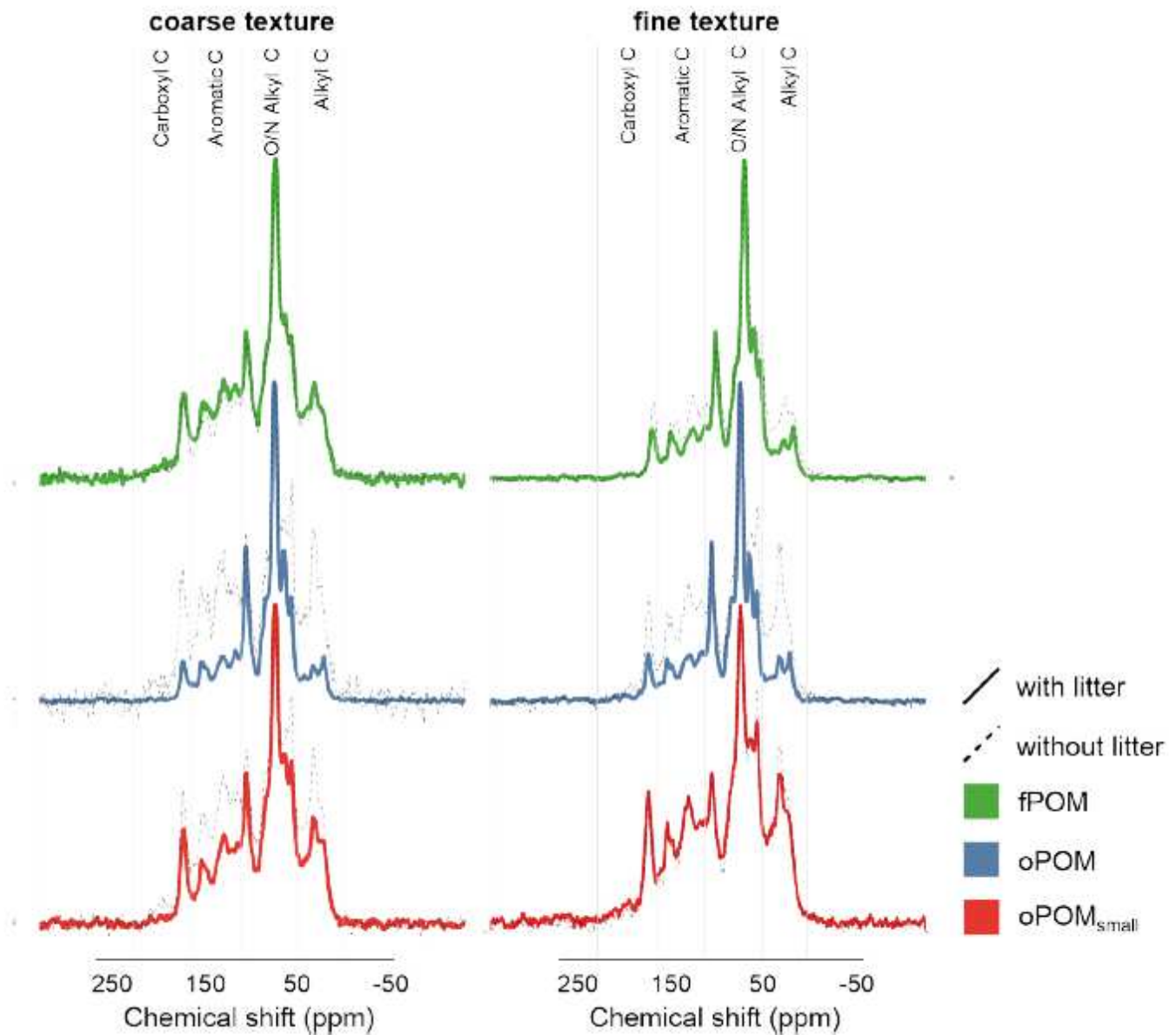


**Figure 3**

Differences in the chemical composition of particulate OM fractions. Solid-state  $^{13}\text{C}$ -CP-MAS NMR spectra displaying the chemical compositions of free POM (fPOM) and occluded POM (oPOM, oPOM<sub>small</sub>) in coarse- and fine-textured soil (control samples in black). The chemical shift regions represent the following functional groups: 0-45 ppm (alkyl C), 45-110 ppm (O/N alkyl C), 110-160 ppm (aromatic C), and 160-220 ppm (carboxyl C).  $n = 3$  for the following fractions: fPOM with litter (both textures), oPOM with litter (both textures), oPOM<sub>small</sub> with litter in the finer texture. For the rest of the samples,  $n = 1$ .

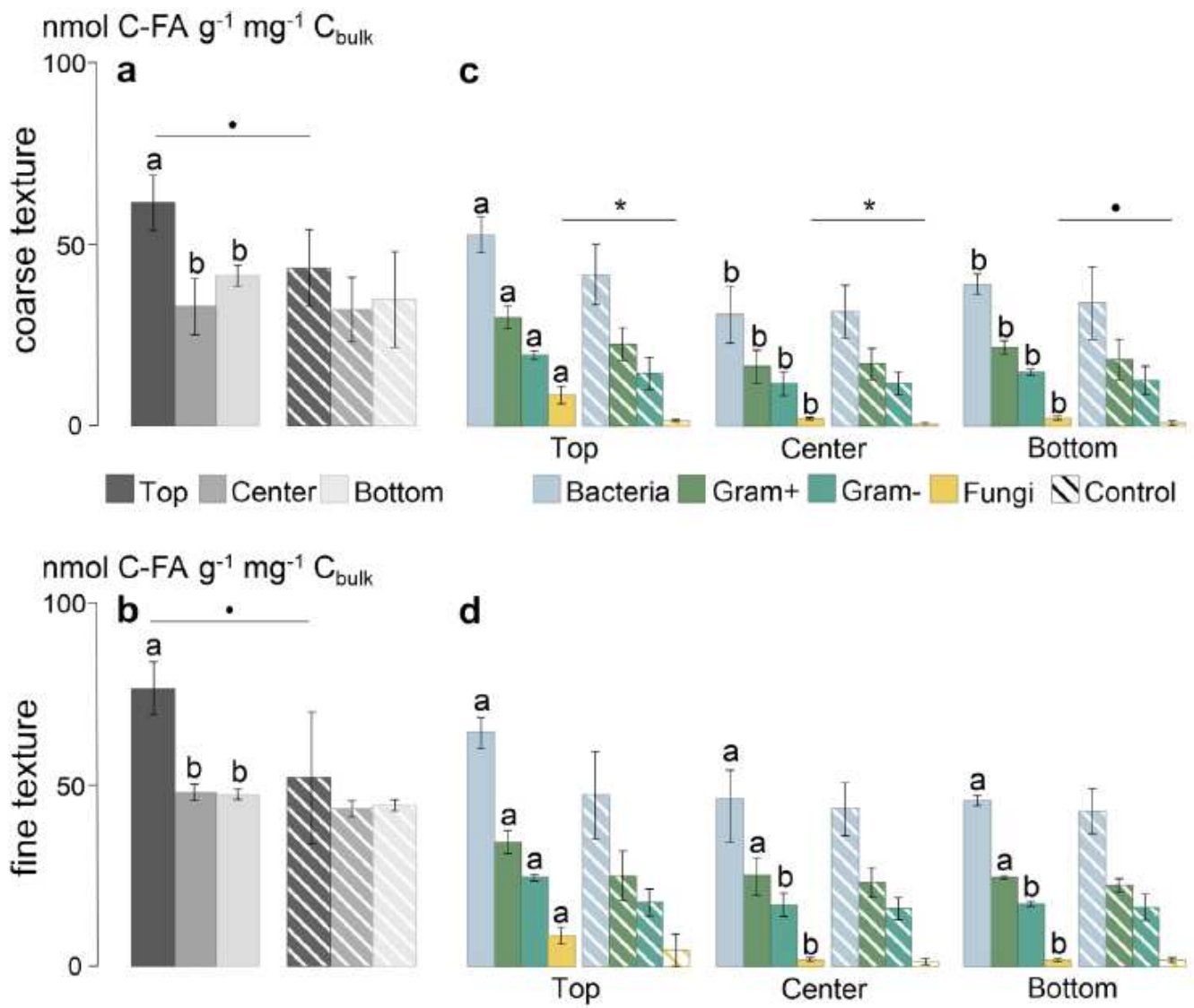


**Figure 4**

Community structures and functionality of microorganisms. The total abundance of phospholipid fatty acids (PLFA) normalized for bulk C in nmol C-FA g<sup>-1</sup> mg<sup>-1</sup> C<sub>bulk</sub> (means, SDs displayed with errors bars, n = 3) in soil with a coarser and b finer texture, divided into four microbial subgroups in c coarse- and d fine-textured soil. Significance levels indicated by dots and asterisks (\*p < 0.1, \*p < 0.05) represent the differences between the litter treatment and controls, and lowercase letters represent the significant (p < 0.05) differences between the layers. Control samples are displayed as hatched.

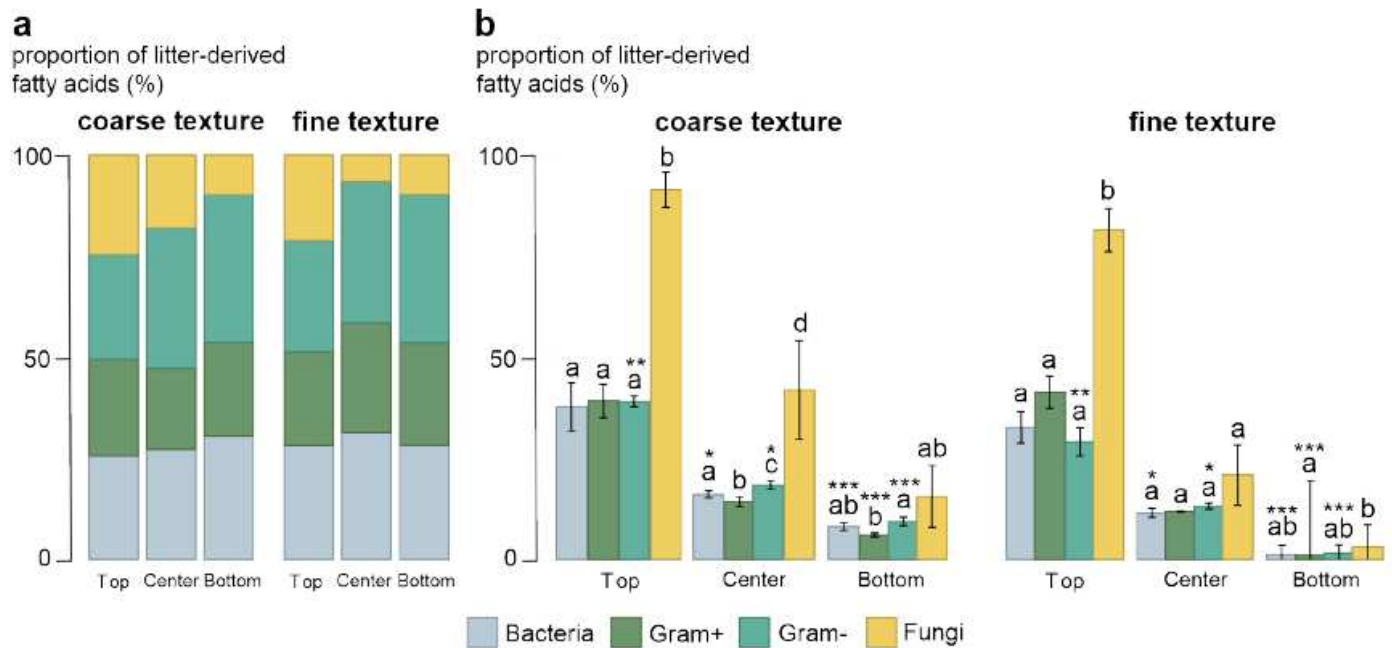


**Figure 5**

Litter incorporation in microbial biomass. a The proportion of litter-derived fatty acids within a certain microbial group related to the total amount of litter-enriched fatty acids in the entire sample (%) in the three depths of two textures (means,  $n = 3$ ). b The proportion of  $^{13}\text{C}$ -enriched fatty acids compared to unlabeled fatty acids within each microbial group (%) in the three depths of two textures (means, SDs displayed with errors bars,  $n = 3$ ). Lowercase letters represent the significant differences ( $p < 0.05$ ) between microbial groups and asterisks ( $*p < 0.05$ ,  $**p < 0.01$ ,  $***p < 0.001$ ) represent the differences between textures. Differences between depths were significant in all groups.

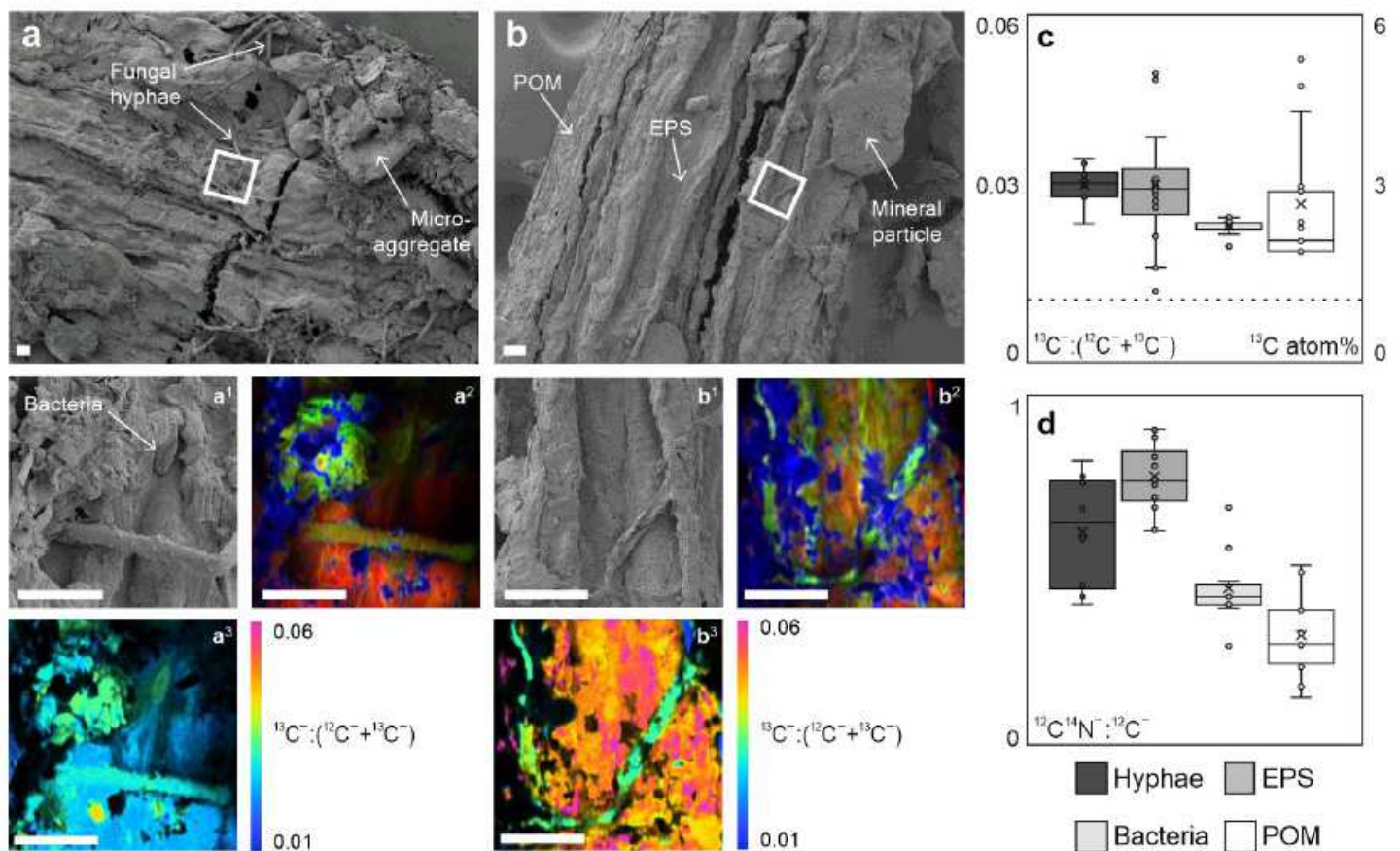


**Figure 6**

High  $^{13}\text{C}$  enrichment detected in fungal hyphae and EPS based on NanoSIMS imaging. Scanning electron microscopy (SEM) images of  $^{13}\text{C}$ -enriched maize litter incubated in microcosms and isolated as particulate organic matter (POM) in a coarse- and b fine-textured soil. a1/b1 SEM micrographs of measurement spots in (a1) coarse- and (b1) fine-textured soil, which were later analyzed by nano-scale secondary ion mass spectrometry (NanoSIMS). a2/b2 NanoSIMS composite images displayed as RGB (Red =  $^{12}\text{C}^-$ , Green =  $^{12}\text{C}^{14}\text{N}^-$  and Blue =  $^{16}\text{O}^-$ ). a3/b3 NanoSIMS hue-saturation intensity (HIS) images displaying the  $^{13}\text{C}^-:(^{12}\text{C}^- + ^{13}\text{C}^-)$  isotope ratios of POM, fungal hyphae and extracellular polymeric substances (EPS) in the coarse- and fine-textured soil. Here the enrichment level is displayed as HIS images with a color scale ranging from natural abundance (0.011) in blue to high enrichment in purple (0.065). Scale bars represent  $10\ \mu\text{m}$ . c Boxplots of  $^{13}\text{C}^-:(^{12}\text{C}^- + ^{13}\text{C}^-)$  isotope ratios and d  $^{12}\text{C}^{14}\text{N}^-:^{12}\text{C}^-$  ratios of hyphae ( $n = 8$ ), EPS ( $n = 16$ ), bacteria ( $n = 10$ ), and POM ( $n = 13$ ) in both textures obtained by NanoSIMS (medians, error bars denote data ranging between the 5th and 95th percentiles). The natural abundance of  $^{13}\text{C}$  is indicated by the hatched line. The regions of interest were selected manually on continuous fragments of hyphae, individual bacteria, patches of EPS and exposed POM surfaces. Significant differences ( $p < 0.05$ ) between the four groups are indicated by lowercase letters.

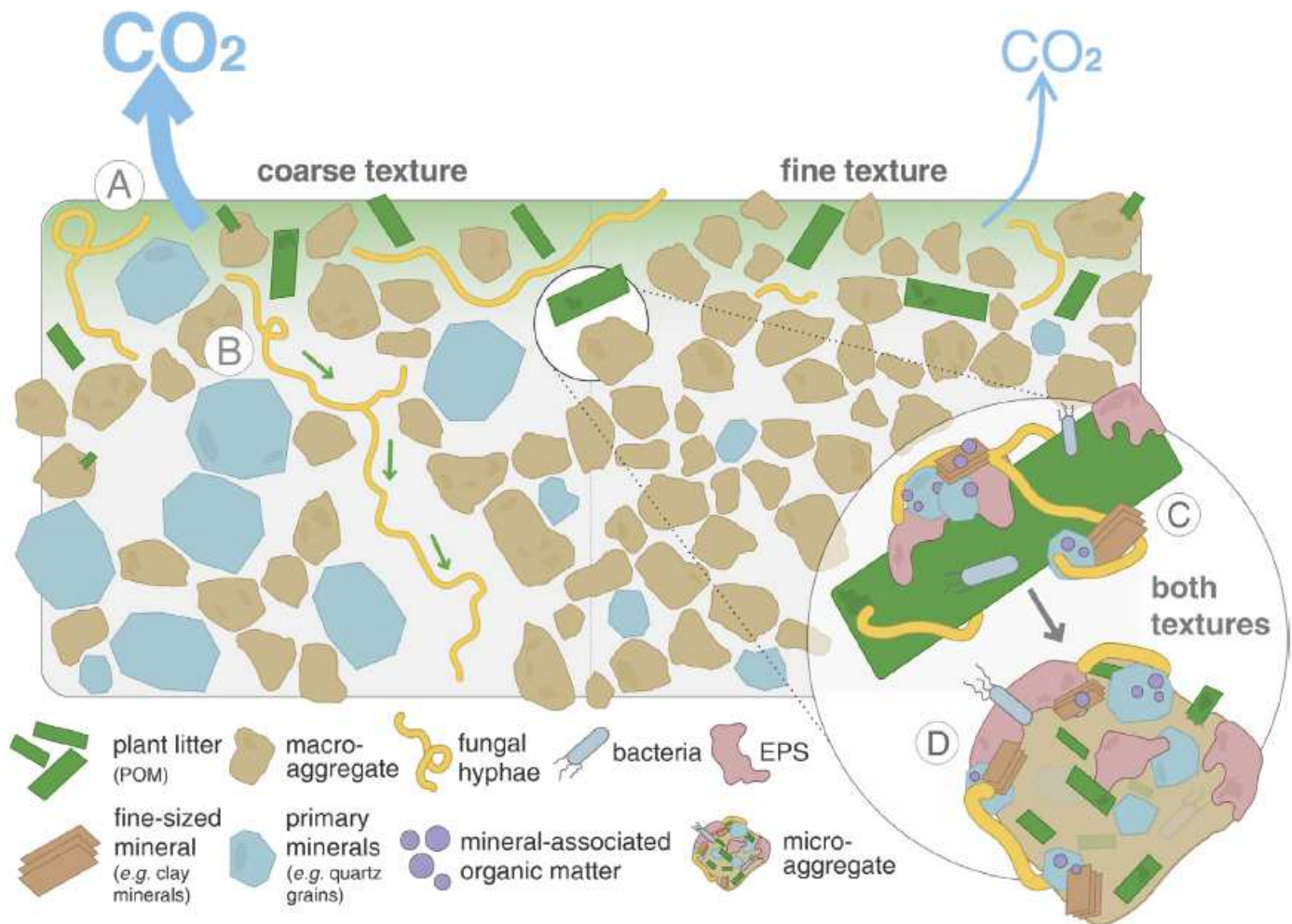


**Figure 7**

Aggregate and mineral-associated organic matter formation in soils of different textures driven by interactions between litter, microorganisms and soil matrix. Fresh litter surfaces serve as hotspots of microbial activity driving the formation of organo-mineral associations in concert with comprising a nucleus for aggregate formation. (A) Coarse soil texture fosters higher mineralization of native and litter-derived organic matter resulting in higher CO<sub>2</sub> emissions compared to the fine-textured soil. (B) Fungal hyphae in coarse-textured soils promote the translocation of litter-derived C away from the litter source. (C) Regardless of texture, gluing of fine-sized minerals, driven by microbial products (EPS) on the fresh litter surface lead to (D) the formation of soil aggregates directly at the plant-soil interface.